Supporting Information for:

Nanocrystals of Lead Chalcohalides: A Series of Kinetically-Trapped Metastable Nanostructures

Stefano Toso[†Δ,∇], Quinten A. Akkerman[†Φ,∇], Beatriz Martín-García[†Γ,∇], Mirko Prato[Σ], Juliette Zito[†], Ivan Infante[†§*], Zhiya Dang[†Θ], Anna Moliterni[‡*], Cinzia Giannini[‡], Eva Bladt[ϫ┼], Ivan Lobato[ϫ┼], Julien Ramade[ϫ┼], Sara Bals[ϫ┼*], Joka Buha[†], Davide Spirito[†ϟ], Enrico Mugnaioli[⊥], Mauro Gemmi[⊥*], Liberato Manna[†*]

[†] Department of Nanochemistry, [Σ] Materials Characterization Facility, Istituto Italiano di Tecnologia, Via Morego 30, 16163 Genova, Italy

[Δ] Dipartimento di Matematica e Fisica and Interdisciplinary Laboratories for Advanced Materials Physics, Università Cattolica del Sacro Cuore, via Musei 41, I-25121 Brescia, Italy

[§] Department of Theoretical Chemistry, Faculty of Science, Vrije Universiteit Amsterdam, de Boelelaan 1083, 1081 HV Amsterdam, The Netherlands

[‡] Istituto di Cristallografia - Consiglio Nazionale delle Ricerche (IC-CNR), via Amendola 122/O, I-70126 Bari, Italy

[ϫ] Electron Microscopy for Materials Science (EMAT), University of Antwerp, Groenenborgerlaan 171, 2020 Antwerp, Belgium

[┼] NANOlab Center of Excellence, University of Antwerp, Belgium

[⊥] Center for Nanotechnology Innovation@NEST, Istituto Italiano di Tecnologia, Piazza San Silvestro, 12, 56127 Pisa, Italy

*E-mail: ivan.infante@iit.it, annagrazia.moliterni@ic.cnr.it, sara.bals@uantwerpen.be, mauro.gemmi@iit.it, liberato.manna@iit.it

Present Address:

[Φ] Department of Chemistry and Applied Biosciences, ETH Zürich, Vladimir Prelog Weg 1, CH-8093 Zürich, Switzerland

[Γ] CIC nanoGUNE, Tolosa Hiribidea, 76, E-20018 Donostia – San Sebastian, Spain

[ϟ] IHP–Leibniz-Institut für innovative Mikroelektronik, Material Research Semiconductor Optoelectronics, Frankfurt (Oder), Germany

[Θ] School of Materials, Sun Yat-sen University, Guangzhou, 510275, China

Contents:

Support Material

a) Direct synthesis of $Pb_4S_3Br_2$ NCs

The $Pb_4S_3Br_2$ nanocrystals (NCs) used in this work have been synthesized via a modification of the heat-up method previously published by our group.[1] In a standard synthesis, 0.2 mmol of $PbBr_2$ and 0.2 mmol of $Pb(SCN)_2$ were dissolved in a mixture of 10 mL ODE and 250 µL of OLAM and OA at 110°C in a 25 mL three-necked flask. This temperature was not exceeded during the solubilization, to avoid triggering the thermal decomposition of SCN^- ions. Once the two solids were completely dissolved the solution appeared clear and pale-yellow. At that point, the flask was lifted from the heating-mantle, which was overheated to an inner temperature of 250°C to grant the fast increase of temperature required for the synthesis. The flask, till that point kept at ≈110°C by hovering it at the rim of the mantle, was again inserted and as a result the solution quickly heated up (≈ 20°C / min), consequently turning from light-yellow to bloody red above 150°C. As reported in our previous paper, the following reaction is taking place:[1]

$$2\ SCN^- + 3O_2 \rightarrow S^{2-} + SO_2 + 2\ CO_2 + N_2$$

As a consequence, S^{2-} becomes suddenly available in the reaction system and co-precipitates with Pb^{2+} and Br^- forming the reported $Pb_4S_3Br_2$ phase.

Figure S1. Timeline of the reaction for the synthesis of $Pb_4S_3Br_2$ NCs by direct observation of aliquots collecting during the synthesis. Many aliquots of the reaction batch were taken using a syringe and immediately quenched by immersing the vial in a water bath. The quenching temperature increases from left to right, as reported in °C on each vial.

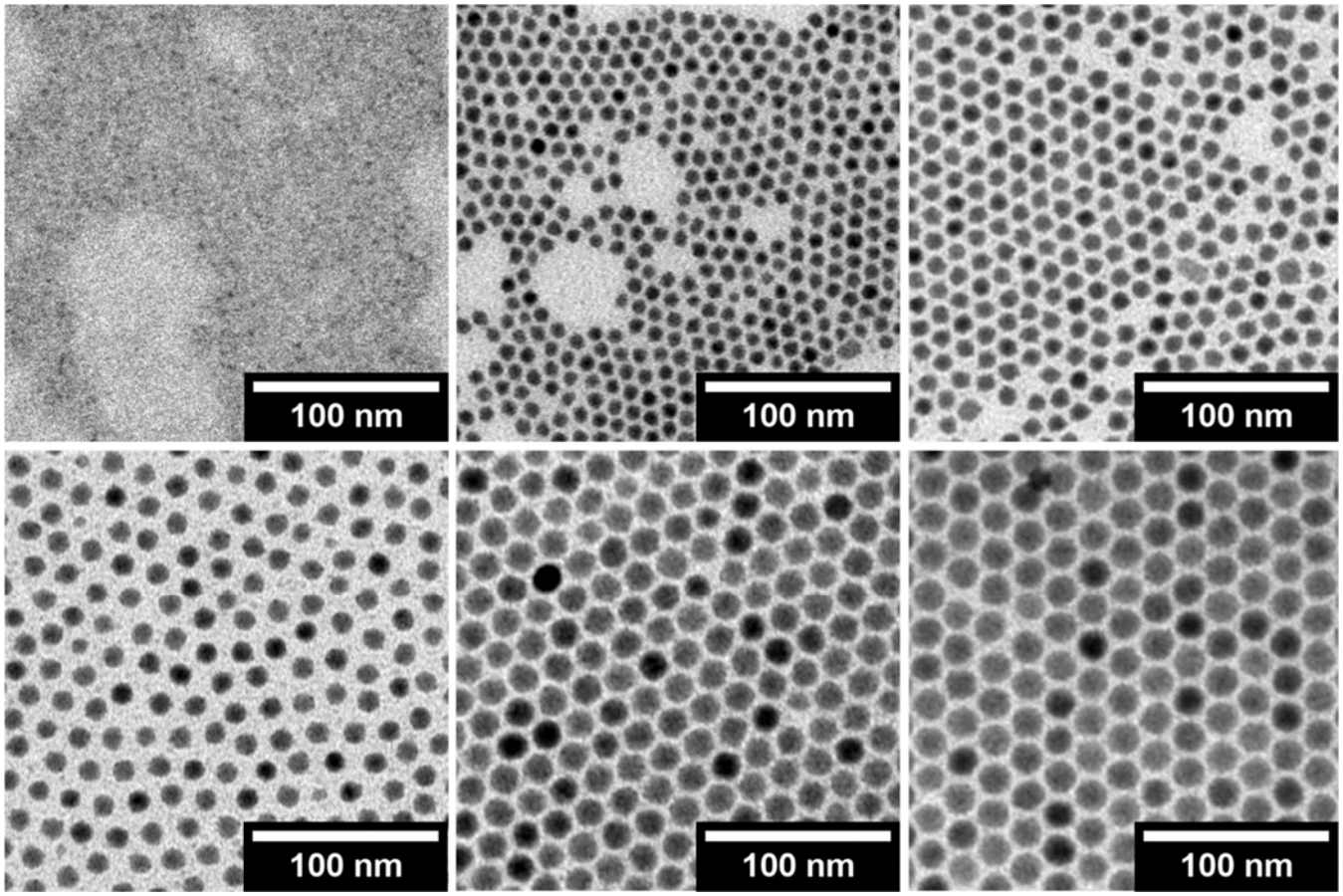

Figure S2. Timeline of the reaction for the synthesis of $Pb_4S_3Br_2$ NCs by TEM. The samples shown here come from the series in Figure S1. The quenching temperature increases from left to right and from top to bottom: 150 – 160 – 165 – 170 – 180 – 190°C.

Table S1. Timeline of the reaction by TEM. Table summarizing the size and size dispersion of $Pb_4S_3Br_2$ NCs obtained by quenching the reaction at different temperatures, together with the time elapsed between the start of sample heating and the quenching.

Quenching Temperature (°C)	Time after heating started (s)	Size ± distribution FWHM (nm)
120	0	no particles
130	28	no particles
140	50	no particles
150	75	no particles
155	88	not measured
160	102	7.8 ± 0.63
165	117	9.46 ± 0.44
170	148	11.54 ± 0.41
180	166	15.33 ± 0.59
190	182	15.99 ± 1.25

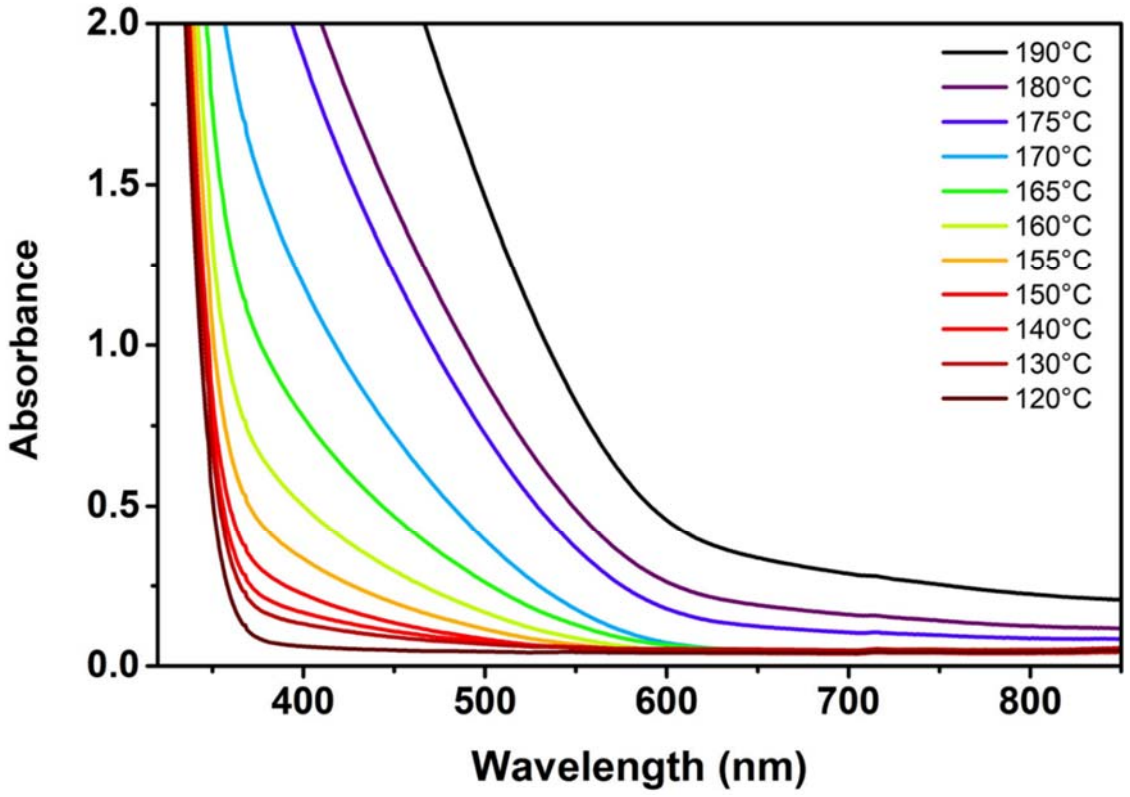

Figure S3. Timeline of the reaction for the synthesis of $Pb_4S_3Br_2$ NCs by optical absorption. Absorption spectra of the aliquots shown in Figure S1. The spectra were not normalized to give additional information on how the absorbance increases while the NCs nucleate and grow. All the samples were prepared by diluting 50 µL of the crude reaction batch in 900 µL of toluene inside a 10 mm-path cuvette. The spectra collected from 175 – 180 – 190°C aliquots show the characteristic effect of scattering, since particles grew too large to form a stable colloidal suspension in toluene once the samples cooled to room temperature and were diluted.

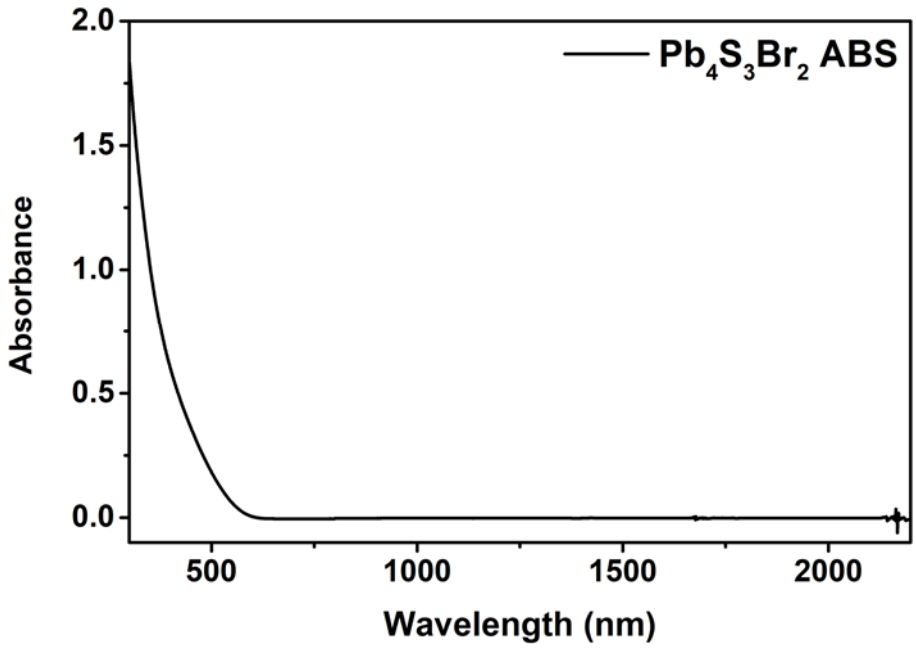

Figure S4. $Pb_4S_3Br_2$ NCs by absorption. Absorption spectrum of $Pb_4S_3Br_2$ NCs extended into the infrared region, demonstrating no absorption beyond ~650 nm.

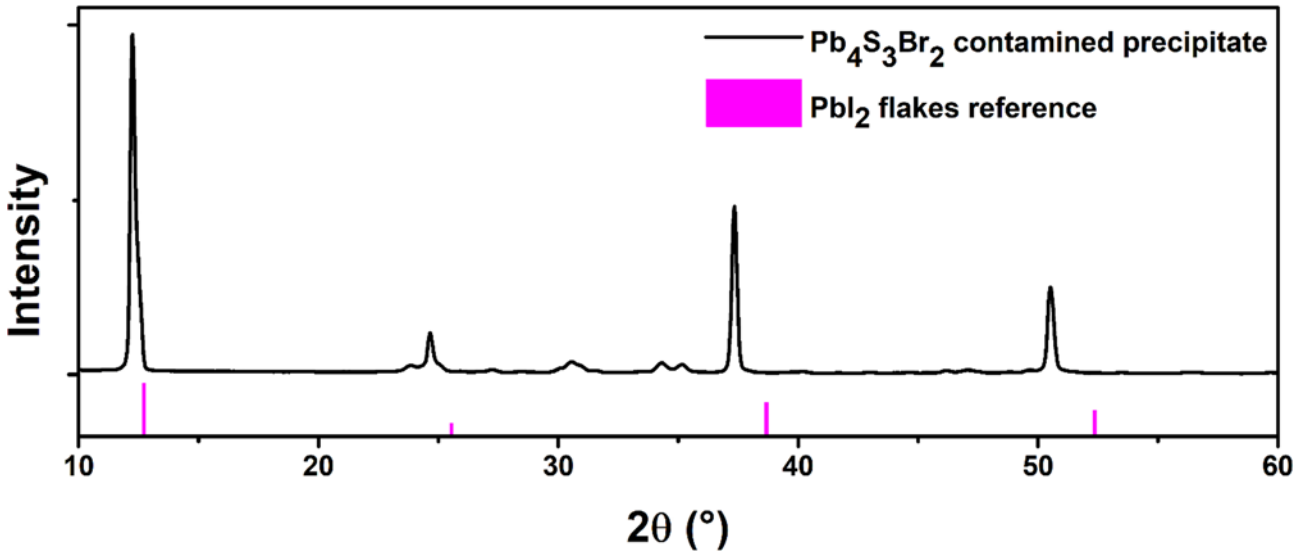

Figure S5. XRPD of contaminated $Pb_4S_3Br_2$ NCs. XRPD pattern of the precipitate formed during a synthesis of $Pb_4S_3Br_2$ NCs which underwent overheating (T≈200°C). The sharp peaks do not belong to $Pb_4S_3Br_2$, whose pattern is barely visible above the baseline, but are instead attributed to yet unreported $PbBr_2$ layered structures. We suspect that they share similarities with the PbI_2 impurity observed for of $Pb_4S_3I_2$ NCs (see Figure S32).[2] The peak shift towards lower angles (larger periodicities) is probably due to a structural distortion.

Further accretion of $Pb_4S_3Br_2$ NCs

Large-size $Pb_4S_3Br_2$ NCs were needed to attempt an *ab initio* NC structure solution via single particle 3D-ED. A batch of NCs was synthesized according to the reported procedure, and the growth was quenched at 170°C. The particles were not recovered from the reaction batch; instead, the flask was re-heated to 170°C and kept stirring at this constant temperature. In a separated flask, 0.6 mmol of $PbBr_2$ and 0.6 mmol of $Pb(SCN)_2$ were dissolved in 30 mL of ODE, 750 µL OLAM and 750 µL OA (3× standard synthesis). The procedure was stopped before the heat-up step. Instead, the liquid was filtered with a 0.2 µm PTFE syringe filter and slowly added dropwise to the hot batch of NCs at a rate of 5 mL/h with a syringe pump. This procedure ensured a steady growth of the pre-existing NCs. In our experiment, the NCs grew from an original 13.1 ± 0.48 nm size (batch already hot and stable at 170°C, no further addition) to a final 27.1 ± 1.90 nm size (after 30 mL, 6 h addition).

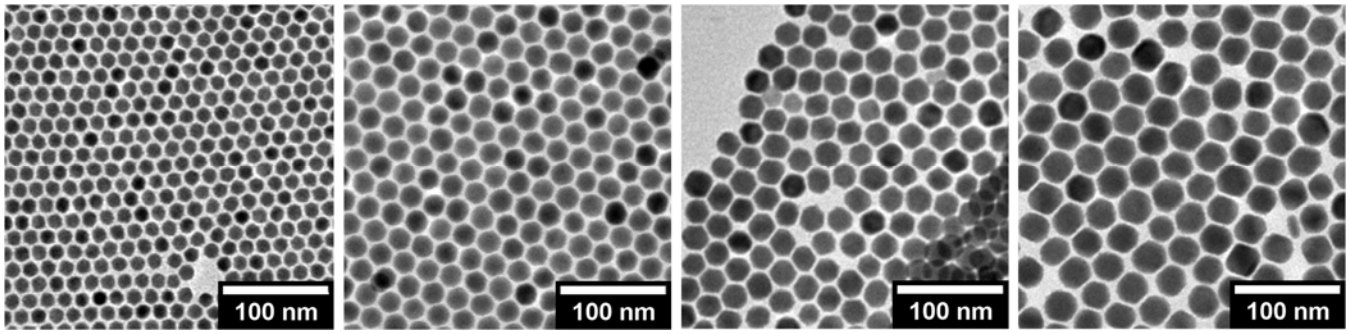

Figure S6. $Pb_4S_3Br_2$ accretion. $Pb_4S_3Br_2$ NCs at various stages of the accretion, evidencing the transition from a non-faceted spherical morphology to a faceted polyhedral one. From left to right: starting NCs originally quenched at 170°C; NCs after an addition of 7.5 mL; 22.5 mL; 30 mL of the accretion precursor solution.

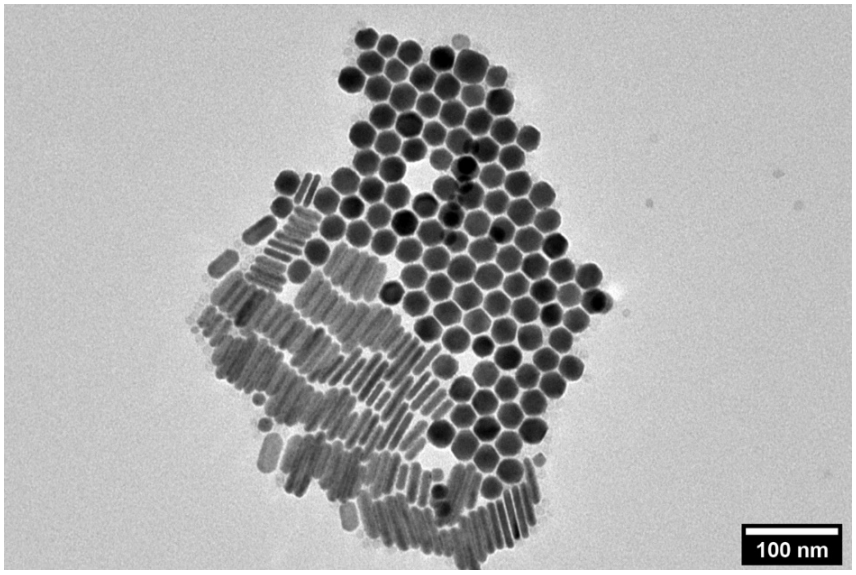

Figure S7. Different $Pb_4S_3Br_2$ morphologies. TEM image showing both the accreted $Pb_4S_3Br_2$ NCs and the $Pb_4S_3Br_2$ nanoplatelets which formed as a side-product during the accretion process.

The compositions of both pseudospherical and platelet-shaped NCs were measured via TEM-EDX and were found in good agreement with each other, suggesting that NCs and nanoplatelets share the same stoichiometry. When comparing the two measurements, one must take into account that the two morphologies will be differently affected by the surface termination and preferential growth effects, thus making it unlikely that the overall elemental compositions will be identical for the two different NC morphologies.

Table S2. TEM-EDX on NCs and platelets. Compositional analysis by TEM-EXD for the pseudospherical and platelet-shaped NCs.

	Pb (at. %)	**S (at. %)**	**Br (at. %)**
$Pb_4S_3Br_2$ NCs	45.76 ± 8.85	28.89 ± 0.64	25.37 ± 1.63
$Pb_4S_3Br_2$ nanoplatelets	38.61 ± 8.36	35.20 ± 0.77	26.19 ± 1.80

b) XPS analysis on the $Pb_4S_3Br_2$ NCs as synthesized.

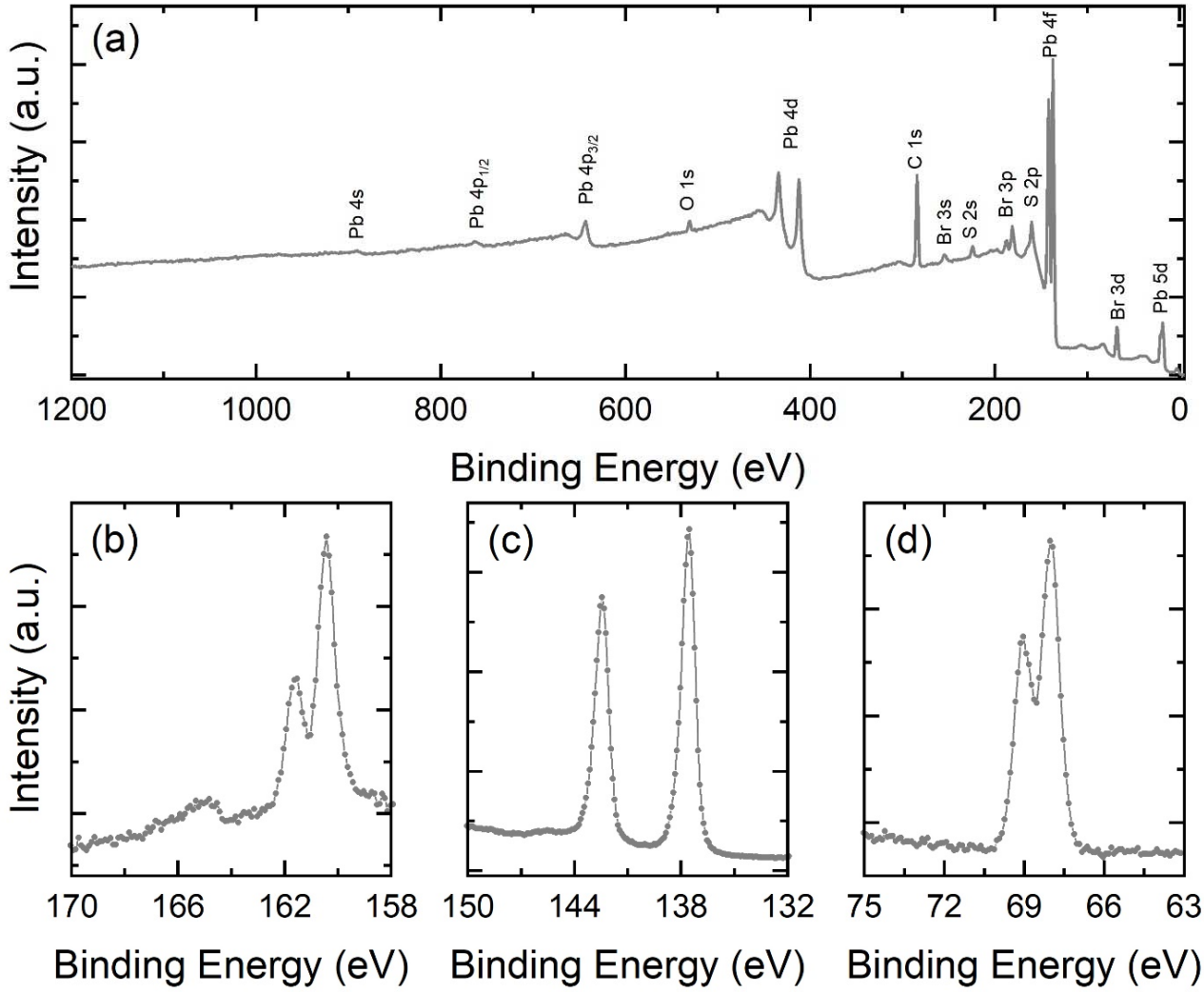

Figure S8. XPS analysis on the $Pb_4S_3Br_2$ NCs as synthesized. a) Wide scan, showing signals due to Pb, S, Br (from the inorganic core of the NCs) together with C and O ones, arising from the organic ligands and possibly also from environmental contaminations, which is common for on samples exposed to moist air. b-d) High resolution scans on the S 2p, Pb 4f and Br 3d energy regions.

Figure S8 reports the XPS data collected on a representative $Pb_4S_3Br_2$ sample. As shown in the wide scan of Figure S8a, the sample is characterized by the presence of Pb, S and Br, together with C and O. These last two elements can be attributed to the organic ligand shell surrounding the inorganic core of the as-synthesized NCs. However, we cannot completely exclude the additional presence of environmental contaminations, due to exposure of the sample to moist air before the XPS data acquisition. Figure S8b-d show the high-resolution spectra for the main XPS lines of S, Pb and Br, respectively. The S 2p spectrum in Figure S8b is characterized by an intense doublet on the low binding energy side of the investigated range (main component centered at 160.4 ± 0.2 eV) and by a low intensity signal in the 165 – 167 eV

energy range. The main doublet is in a position close to that reported in literature for sulfides;[3] in particular, sulfur in PbS is typically reported having the main S 2p component at 160.6 ± 0.6 eV. The low intensity signal, instead, is at a position that has been reported for instance for elemental S or for S bound to C in organic molecules,[3] thus suggesting that it could be attributed to synthesis byproducts that were left with the sample after the washing procedure. The Pb 4f spectrum in panel (c) shows the presence of a single doublet, with the main component centered at 137.6 ± 0.2 eV. The position is typical of Pb(II) compounds, and in particular Pb in PbS is typically reported having the main Pb 4f component at 137.8 ± 0.4 eV.[3]The Br 3d spectrum in Figure S8d shows the presence of a single doublet, with the main component centered at 68.0 ± 0.2 eV. This position is typical of bromides.[3]

Similar results were obtained on all the investigated batches; the following table reports the results of the quantitative analysis.

Table S3. XPS analysis on four different batches of $Pb_4S_3Br_2$ NCs as synthesized.

Batch	Pb (at%)	S (at%)	Br (at%)
1	43.30	31.70	25.00
2	42.70	33.70	23.70
3	40.60	32.60	26.80
4	46.80	30.60	22.50
Average	43.35	32.15	24.50
St. dev.	2.23	1.14	1.60

The reported values, together with the oxidation states obtained for Pb, S and Br, point to a $Pb_4S_3Br_2$ stoichiometry for the obtained compound (Pb:S:Br = 44.4:33.4:22.4).

c) EDX analysis on as synthesized $Pb_4S_3Br_2$ NCs.

One of the NC suspensions used to prepare the solar cells was analyzed via SEM-EDX to measure the NCs composition. For the elemental analyses the Pb-L spectral line (10.551 eV) was used instead of the default Pb-M (2.34 eV), which overlaps with the S-K line (2.309 eV). This avoided the need for a deconvolution and produced results in line with those obtained by XPS, in good agreement with the expected $Pb_4S_3Br_2$ stoichiometry (Pb:S:Br = 44.4 : 33.3 : 22.2).

Table S4. SEM-EDX analysis on as synthesized $Pb_4S_3Br_2$ NCs.

Batch	Pb (at%)	S (at%)	Br (at%)
1	43.39	30.71	25.9
2	43.29	30.27	26.43
3	43.46	29.09	27.45
4	42.44	29.29	28.27
Average	43.16	29.84	27.013
St. dev.	0.48	0.78	1.06

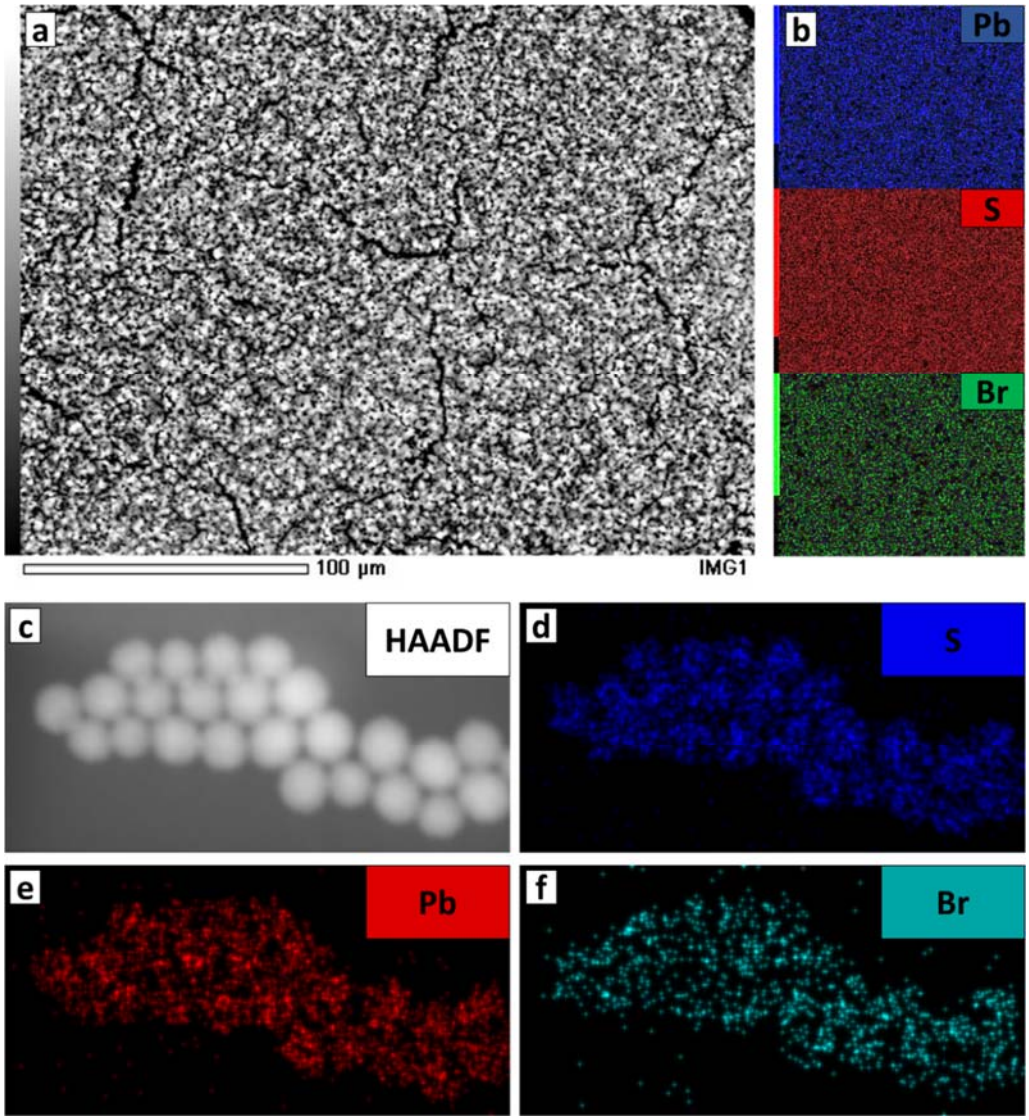

Figure S9. a) Backscattered electrons image of one area of the $Pb_4S_3Br_2$ NCs film prepared for the SEM-EDX elemental analysis, together with b) the corresponding elemental maps. c) HAADF-SEM imaging of a cluster of $Pb_4S_3Br_2$ NCs, together with d-f) the corresponding EDX compositional maps, showing that the elements are uniformly distributed in the NCs.

d) TGA analysis on $Pb_4S_3Br_2$ NCs.

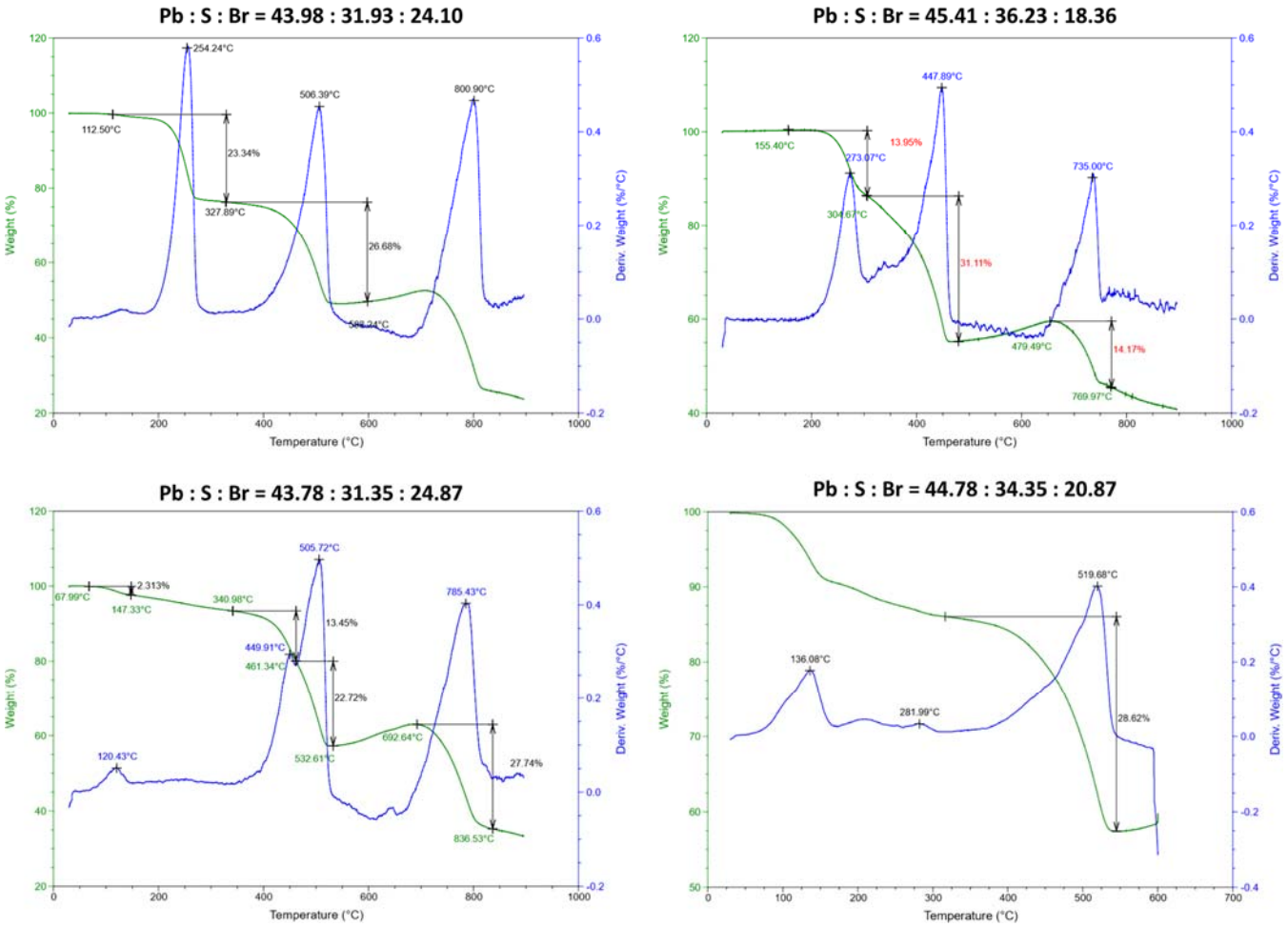

Figure S10. TGA analysis on $Pb_4S_3Br_2$ NCs. Four TGA ramps measured on four different samples, together with the composition extracted from each analysis.

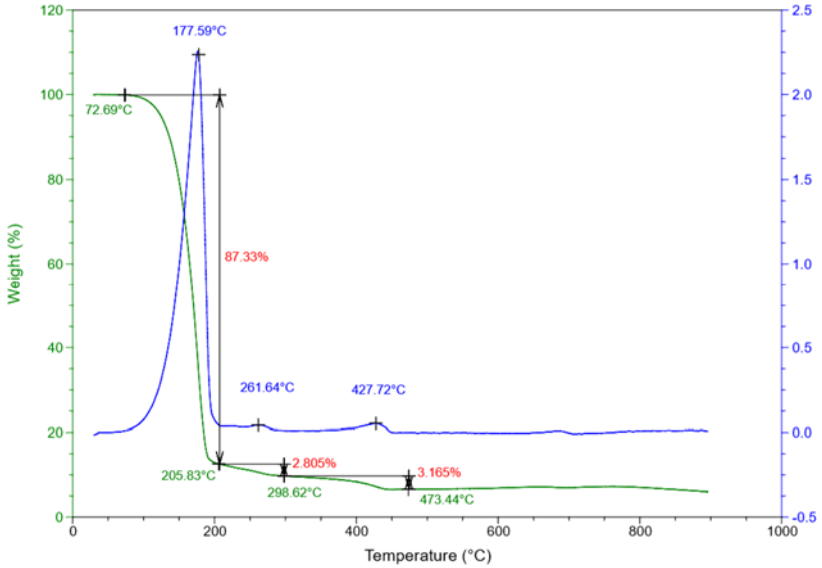

Figure S11. TGA analysis on a non-washed sample $Pb_4S_3Br_2$ NCs. TGA control experiment performed on a non-washed sample (therefore rich in the organic fraction) right after the synthesis. The huge mass loss in the temperature range 70 – 210 °C is due to the evaporation of high boiling point solvent and ligands (ODE, OLAM, OLAC, T_{eb} = 315 – 364 °C).

Figure S10 shows the outcome of the four TGA experiments we used to provide an estimate of the stoichiometry of the NCs based on a "bulk" measurement. We want to point out that the first mass loss, occurring in a temperature range of 110 – 300°C, represents the desorption/decomposition of the organic fraction in the sample (solvent, ligands) and is therefore heavily sample-dependent. For example, the sample in Figure S11 had not been washed, and the first mass loss accounted for a huge 87% of the total. The bottom left sample in figure S10 contained instead the largest particles that we were able to prepare (~30 nm diameter) and had been cleaned carefully. Indeed, the first mass loss in this case accounted for less than 10% of the total.

The second mass loss, combined with the XRD analyses of the sample after the first mass loss and after the second mass loss, carries the compositional information. The stoichiometry was measured from each dataset according to the following method. We first accurately determined the residual relative masses according to the graphical method shown in Figure S12.

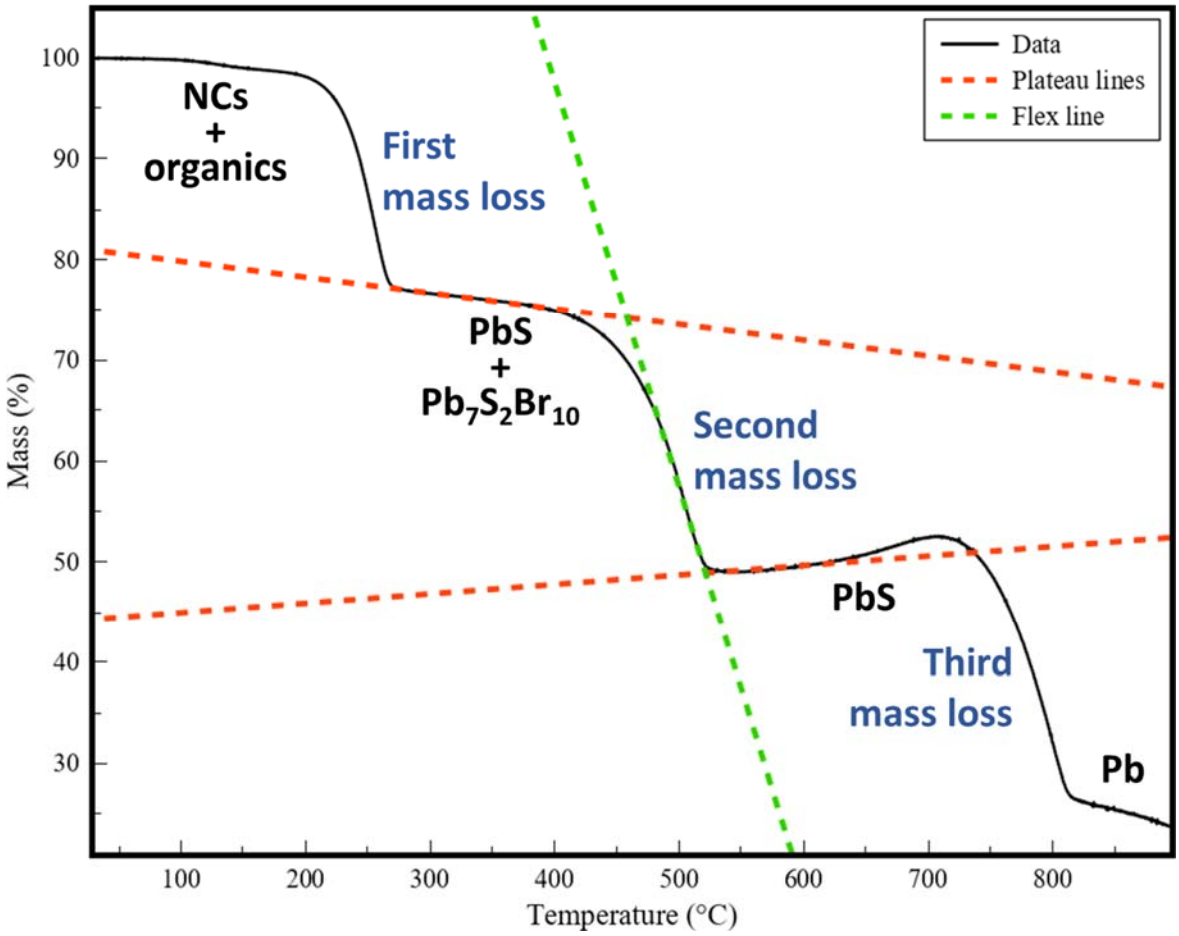

Figure S12. Accurate determination of the initial and final points of the mass loss step. The plateau regions before and after the mass loss were approximated as straight lines tangent to the plot (red lines) as well as the transition slope (green line). The residual relative masses before and after the weight loss were measured at the intersection points between the green and the red lines.

We know from XRPD that, after the first mass loss, the sample contains a mixture of PbS and $Pb_7S_2Br_{10}$, in an unknown molar ratio x: y, that is $x\ PbS + y\ Pb_7S_2Br_{10}$. Assuming that in the first mass loss only the organic fraction is removed, the stoichiometry of our initial NCs, in terms of x and y, is $Pb_{x+7y}S_{x+2y}Br_{10y}$. In the second mass loss, $Pb_7S_2Br_{10}$ decomposes to PbS and $PbBr_2$, with the latter sublimating, as the only final product left is PbS. The overall sequence of the two reactions, can then be written as:

$$Pb_{x+7y}S_{x+2y}Br_{10y} \rightarrow x\ PbS + y\ Pb_7S_2Br_{10} \rightarrow 5\ yPbBr_2 \uparrow + (x+2y)\ PbS$$

We determine y by the mass loss of the second step, since only $PbBr_2$ sublimates in this step. We then determine x, since we now know experimentally both y and the total mass of PbS left at the end of the second step. From x and y we then determine the stoichiometry of our initial NCs. This estimate was done on four separate TGA+XRD analyses, run on four different samples. The resulting stoichiometries are reported in the following table.

Table S5. Results of the TGA-based compositional analysis.

Measurement	Pb (at%)	S (at%)	Br (at%)
1	43.98	31.93	24.10
2	43.78	31.35	24.87
3	45.41	36.23	18.36
4	44.78	34.35	20.87
Average	44.49	33.46	22.05
St. dev.	0.75	2.26	3.01

e) Electron beam damage effects during high resolution HAADF-STEM image acquisition

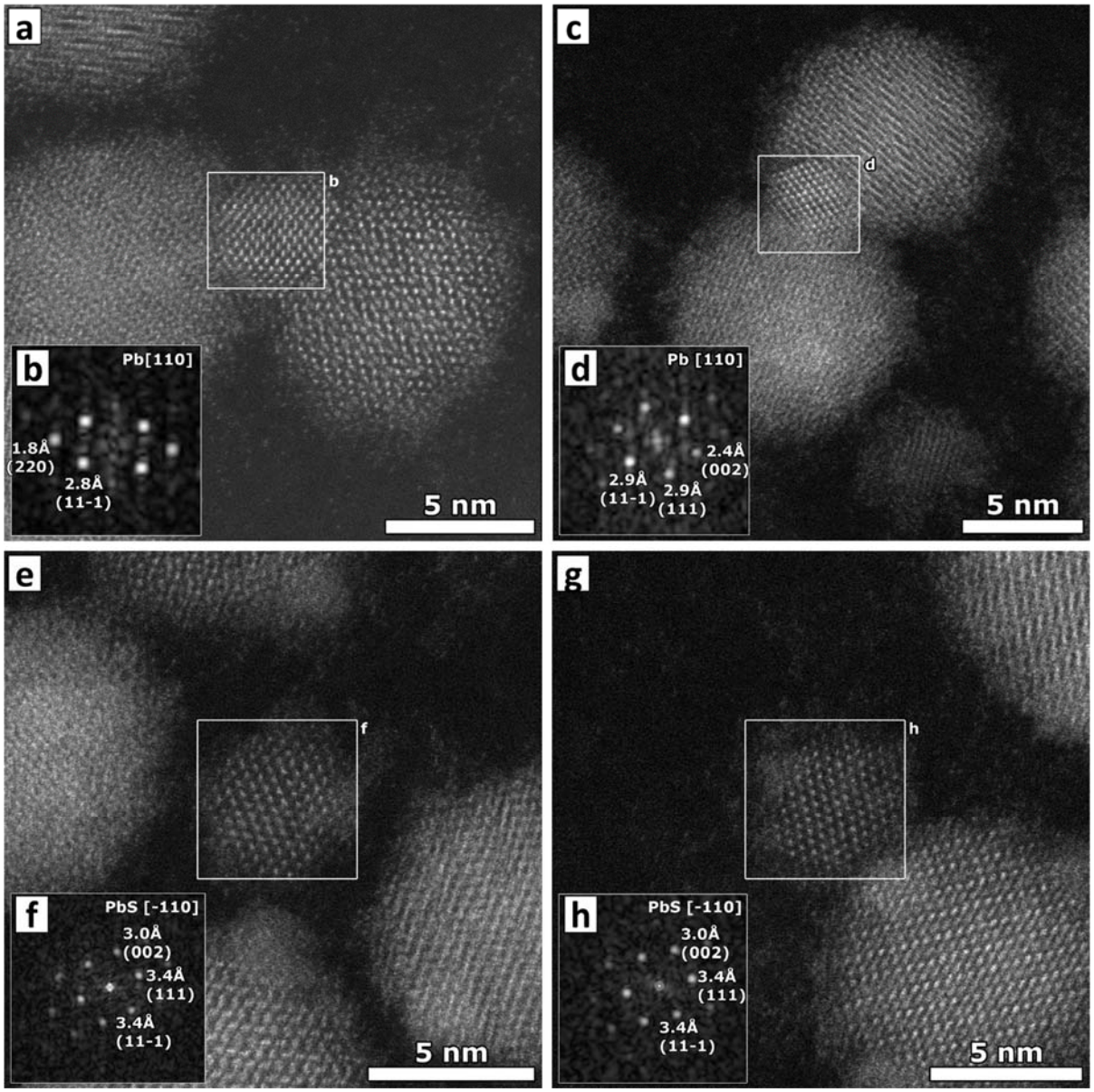

Figure S13. Beam damage during STEM images acquisition. STEM images of the $Pb_4S_3Br_2$ NC together with the Pb (a-c) and the PbS (e-g) NCs formed because of the electron beam-induced damage. The phase of the Pb and PbS NCs was determined *via* atomic lattice distance matching with the help of the calculated Fourier transforms (insets b-d-f-h).

f) *Ab initio* structure solution from 3D-ED data

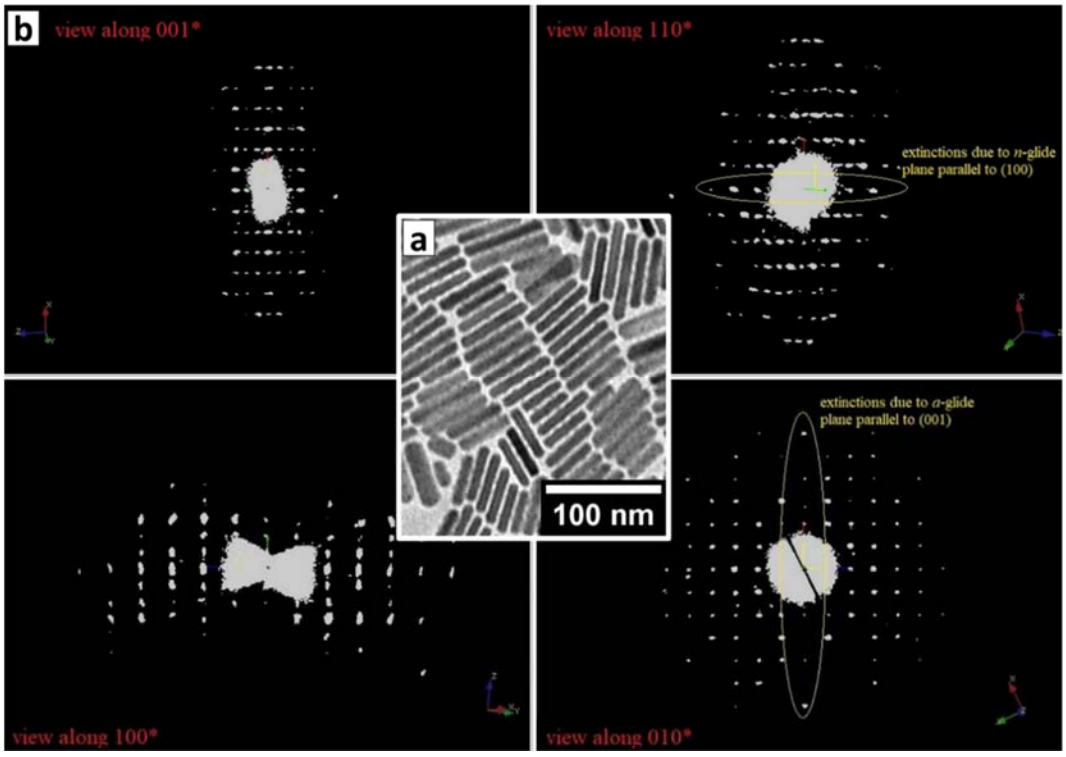

Figure S14. 3D-ED on $Pb_4S_3Br_2$ nanoplatelets. a) TEM image of the $Pb_4S_3Br_2$ nanoplatelets investigated via 3D-ED, together with b) the 3D reconstruction of the reciprocal space of a nanoplatelet viewed along four main reciprocal directions, showing the systematic extinctions exploited for the space group determination.

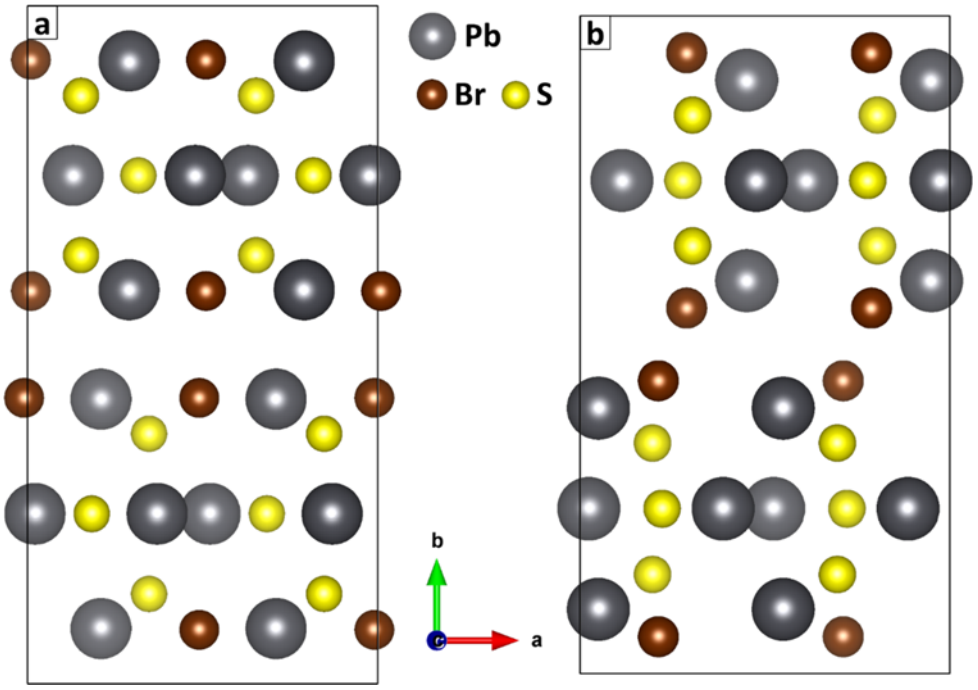

Figure S15. NC and nanoplatelet 3D-ED. A view along the *c* axis of the structural models obtained from the nanoplatelets (a) and from the pseudo-spherical NCs (b). The structures are shown without bonds because, due to the different interatomic distances, different bonds would have appeared, thus complicating the comparison. Due to the low-quality of the data collected on spherical NCs the atomic layout in cell b is unreliable, and the unit cell parameters only were considered. Still, a qualitative match can be recognized between the two structures.

Table S6. Experimental data and 3D-ED structure solution parameters for $Pb_4S_3Br_2$ nanoplatelets.

Crystallographic details	
Unit cell content	$Pb_4S_3Br_2$
Space group	*Pnma*
a, Å	8.0(2)
b, Å	15.5(3)
c, Å	7.9(2)
Cell volume, Å^3	980(40)

3D ED data collection	
Mode	Step-wise with precessing beam
Exposure, s	1.0
Tilt range, °	71.0
Tilt step, °	1.0
Precession angle, °	1.0

Ab initio structure determination in *Pnma* (SIR2014)	
Data resolution, Å	0.9
N° sampled reflections	2030
N° independent reflections	470
Independent reflection coverage, %	65
R_{sym}, %	16.67
R_{SIR}, %	30.58

g) 3D-FT of the crystal structure extracted from the atomic-resolution tomography

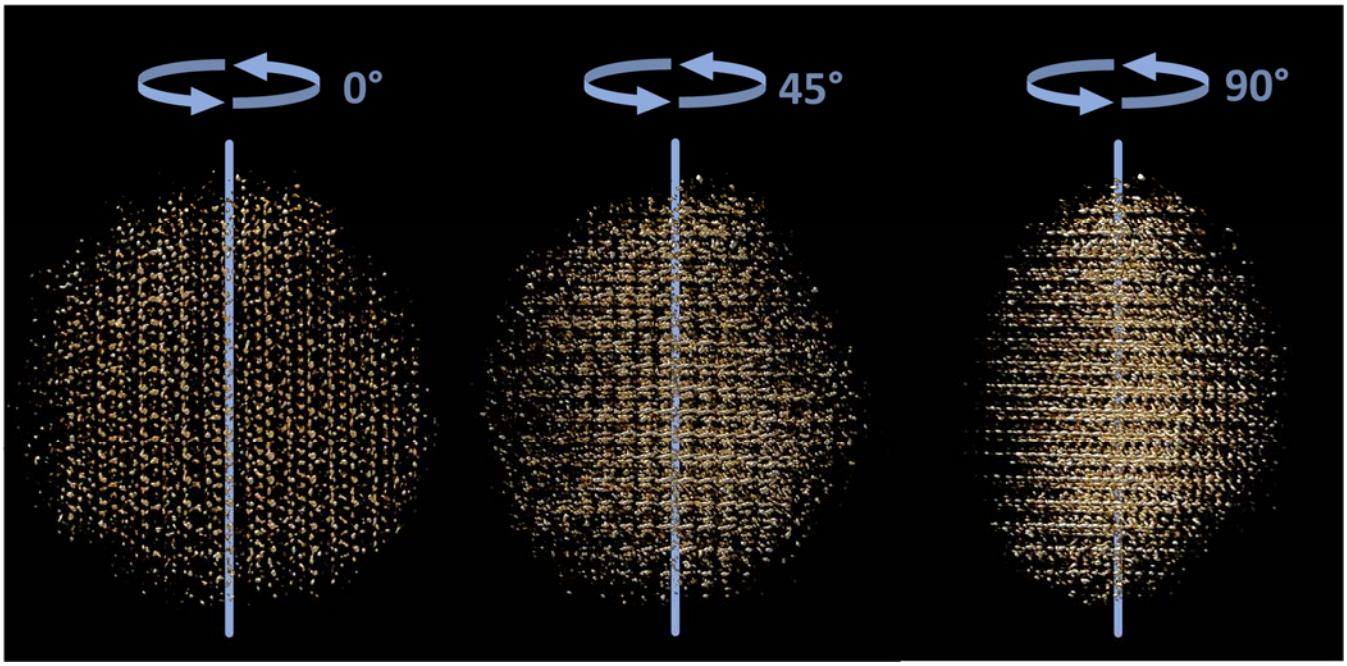

Figure S16. High resolution electron tomography of a NC. The 3D reconstruction of a NC is visualized along three different directions as also seen in Movie_S1. This reconstruction was used to calculate the 3D-FT shown in Movie_S2.

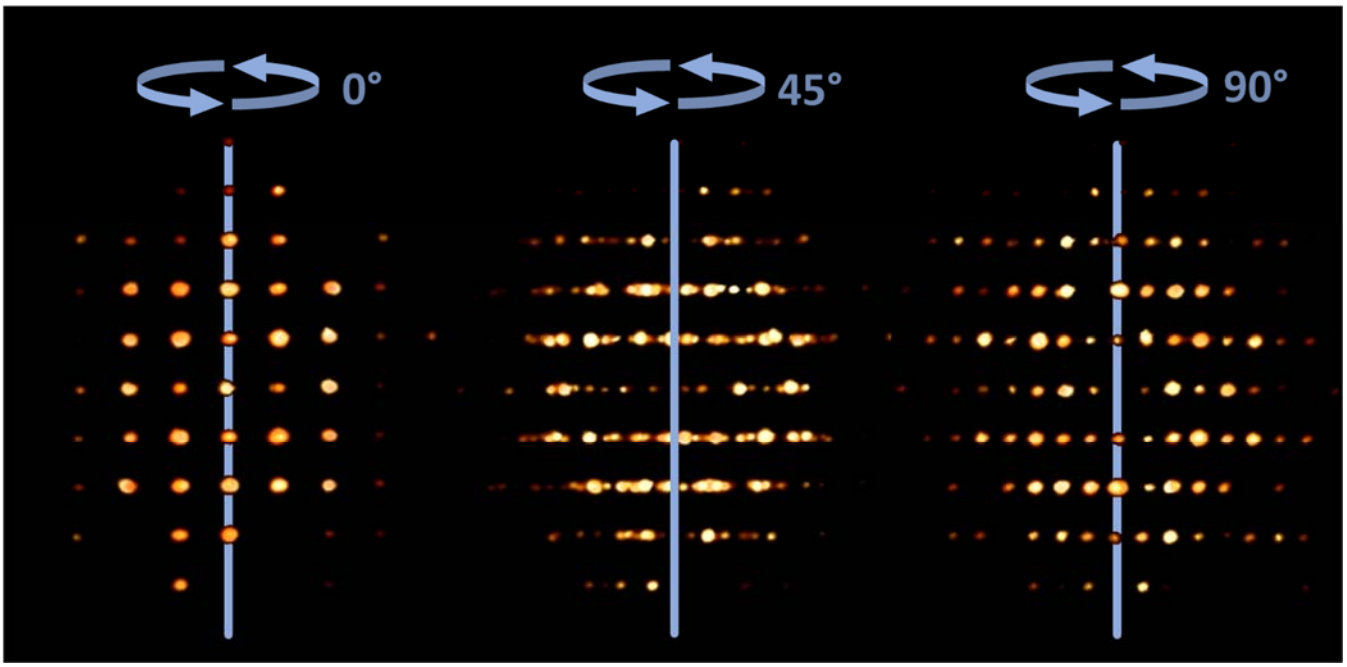

Figure S17. Masked 3D-FT. Starting from the direct-space 3D model shown in Movie_S1, we calculated the (raw) 3D-FT shown in Movie_S2. This data set was subsequently filtered to remove noise and interferences by applying a mask built with the help of the unit cell parameters measured by 3D-ED. The outcome of this procedure is shown in this figure and in Movie_S3.

The direct space electron tomography reconstruction of the NCs, its raw 3D-FT and the filtered version of the 3D-FT are available to the reader in the form of the Movie_S1, Movie_S2 and Movie_S3.*avi* video files.

h) *Ab initio* structure solution from XRPD data

Indexing.

The determination of the cell parameters, the first crucial step of the *ab initio* structure solution, was carried out by EXPO2014,[4] providing to the indexing program N-TREOR09[5] 28 observed peak positions in the 12°-89° 2θ range. Due to the large broadness of the experimental peaks and the consequently unavoidable low accuracy of peak positions, and in order to be able to find the correct cell among the possible ones, the indexing process was carried out in a non-default way by increasing the tolerance concerning the errors on peak positions and the maximum allowed number of unindexed lines. In a default indexing run of N-TREOR09 a plausible cell is characterized by a value of the M_{20} de Wolff figure of merit[6] and of the maximum number of unindexed lines (NIX) equal to or larger than 10 and not greater than one, respectively. In case of the NC powder diffraction pattern, the thresholds on the minimum allowed value of M_{20} and on the maximum tolerated value of NIX were set to 6 and 3, respectively. The less restrictive indexing criteria unavoidably increased the number of possible cells compatible with the experimental data and, at the same time, enabled to include also the correct one, an orthorhombic cell (cell parameters a=8.157862 Å, b=14.849445 Å and c=8.124080 Å), characterized by M_{20} and NIX values equal to 6 and 2, respectively. To recognize the correct cell among the set of candidate cells, the indexing results concerning the orthorhombic cell determined by the 3D electron diffraction study were taken into account.

Space group determination.

The space group determination process by EXPO2014 exploits the information on cell parameters, integrated intensities (extracted in the space group having the largest Laue symmetry and no extinction conditions, *i.e*., in *Pmmm*) and expected unit cell content, to carry out a statistical analysis on suitably weighted integrated intensities, in order to detect systematic absences and calculate a probability value associated to the different possible extinction symbols compatible with the identified crystal system[7–9]. Due to the broad and overlapping peaks in the NC powder pattern and, consequently, to the large errors on the integrated intensities estimates, the results of the statistical study were unreliable and prevented the correct identification of the space group. In case of the 3D-ED data, the greater accuracy of the integrated intensities enabled to detect the absence of:

i) The class of reflections (0 k l) with k+l odd (*i.e.,* the presence of a glide *n* normal to the *a* axis)

ii) The class of reflections (h k 0) with h odd (*i.e.,* the presence of a glide *a* normal to the *c* axis)

This led to the identification of the space group *Pnma*. This result, derived by the investigation based on 3D electron diffraction data, was actively used for the structure solution step by powder diffraction data.

Full pattern decomposition.

EXPO2014 estimates the integrated intensities of reflections by alternating the application of the Le Bail algorithm[10] to least-squares cycles minimizing the residual between observed and calculated profiles. The default profile function used to describe the peak shape is the Pearson VII. The refined variables are scale factor, background coefficients, 2θ-zero shift, peak asymmetry, FWHM parameters, the *m* parameter of the Pearson VII function and the unit cell parameters. Thanks to a useful property of the Le Bail algorithm, to improve the integrated intensities estimates EXPO2014 can fruitfully take advantage of some prior information[11], including the expected positivity of the Patterson function[12] that is particularly effective in case of structures with heavy atoms; for that reason, it was exploited in case of the NC powder diffraction pattern.

Structure solution and structure model optimization.

The default structure solution process by EXPO2014 is based on the application of Direct Methods (DM), providing 20 sets of phases processed by the ALLTRIAL procedure[4], that, for each set of stored phases, automatically performs a preliminary refinement and structure model optimization by a Fourier recycling approach[13]; the corresponding 20 structure models were carefully analyzed by a graphical inspection. The structure model showing the most plausible chemical environment of the Pb atoms (in terms of heavy-atom coordination and interatomic distances, in agreement with the main crystallochemical rules) and the most plausible crystal packing (*i.e.*, that one characterized by the absence of unreliable voids in the cell or implausible large density of atoms, this last usually due to the presence of false atoms in the model) was selected and improved *via* the EXPO2014 graphic tools, allowing to correct some errors on atom labelling and optimize the position of the Br atom (*i.e.*, by deleting and relocating it *via* the calculation of an additional electron density map using $2F_o$-F_c coefficients, where F_o and F_c are the observed and calculated structure factor modulus, respectively). The asymmetric unit of the crystal structure determined by the *ab initio* structure solution from XRPD data (whose main details are provided in Table S7) and its local environment are shown in Figure S18a and S18b, respectively. The crystal structure reveals itself very similar to that one determined by 3D electron data (see Figure S19, showing a view of the overlay of the crystal structures determined by XRPD and 3D electron diffraction data, represented by red and blue rods respectively). A comparison of the two structure models reveals a root mean square deviation (RMSD) of 0.534 Å between them.

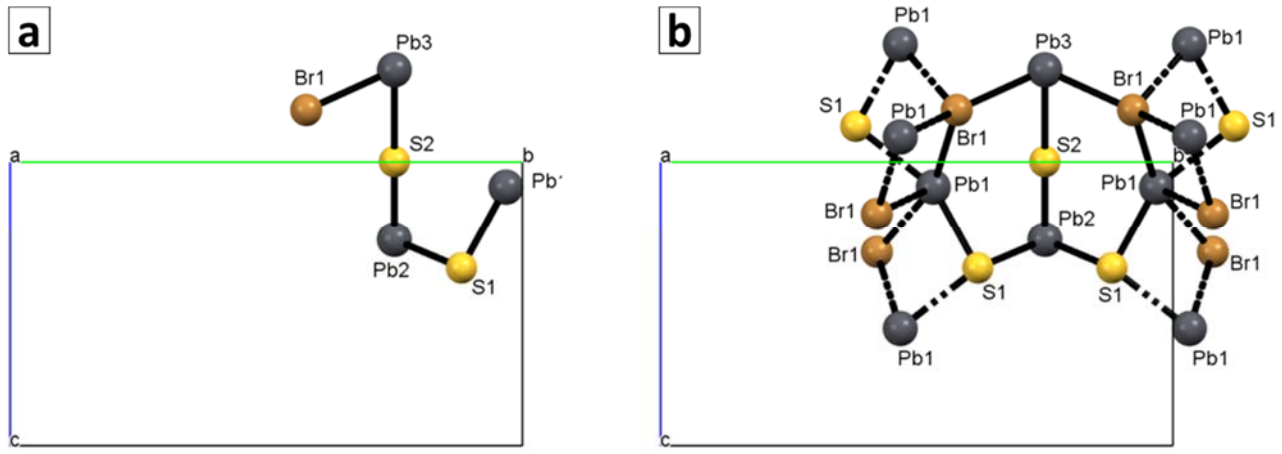

Figure S18. *Ab initio* structure solution from XRPD data. The asymmetric unit a) and its surroundings b) as obtained from the XRPD data-based *ab initio* structure solution.

Table S7. *Ab initio* structure solution from XRPD data. Main crystal data, Wyckoff sites, fractional atomic coordinates, isotropic displacement parameters and geometrical parameters for the XRPD-based *ab initio* structure solution.

Chemical formula	$Pb_4S_3Br_2$
M_r	1084.81
Crystal system, space group	Orthorhombic, *Pnma*
a, *b*, *c* (Å)	8.22592, 14.70843, 8.13988
V(Å^3)	984.847
Z	4
Wavelength (Å)	1.54056
Dx	7.316 mg m^{-3}

Wickoff site, fractional atomic coordinates and isotropic displacement parameters (Å^2)

Atom	*Wick. Site*	*x*	*y*	*z*	U_{iso}
Pb1	8*d*	0.7875	0.9678	0.0879	0.0319
Pb2	4*c*	0.9374	0.7500	0.2740	0.0319
Pb3	4*c*	0.6266	0.7500	−0.3232	0.0319
Br1	8*d*	0.5249	0.5780	−0.1824	0.0619
S1	8*d*	0.6930	0.8809	0.3744	0.0555
S2	4*c*	0.7844	0.7500	−0.0020	0.0025

Geometrical parameters (Å, º).

Pb2—S2	2.5751	S2—Pb3	2.9190
Pb2—S1	2.9011	S1—Pb1	2.7707
Pb2—Pb1	3.7520	Pb3—Br1	2.9006
S2—Pb2—S1	84.67	Pb2—S1—Pb1	82.80
S2—Pb2—Pb1	59.15	Pb2—Pb1—S1	50.10
Pb2—S2—Pb3	177.15	S2—Pb3—Br1	76.96
S1—Pb2—Pb1	47.11		
S1—Pb2—S2—Pb3	138.20	S2—Pb2—Pb1—S1	114.03
Pb1—Pb2—S2—Pb3	95.98	S1—Pb2—Pb1—S1	0.02
S2—Pb2—S1—Pb1	−51.95	Pb2—S2—Pb3—Br1	116.46
Pb1—Pb2—S1—Pb1	0.02	Pb2—S1—Pb1—Pb2	0.02

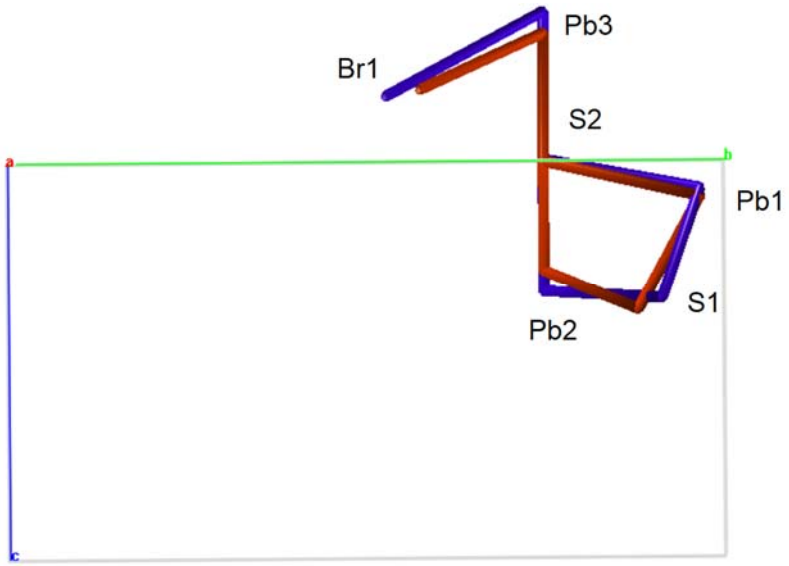

Figure S19. Visual assessment of matching between XRPD and 3D-ED models. Overlay of the asymmetric unities of the structure models obtained by 3D-ED (blue) and by XRPD (red) ab initio structure solution. The root mean square deviation (RMSD) for the two structure models was found to be 0.534 Å.

i) Crystal structures relaxed by DFT calculations

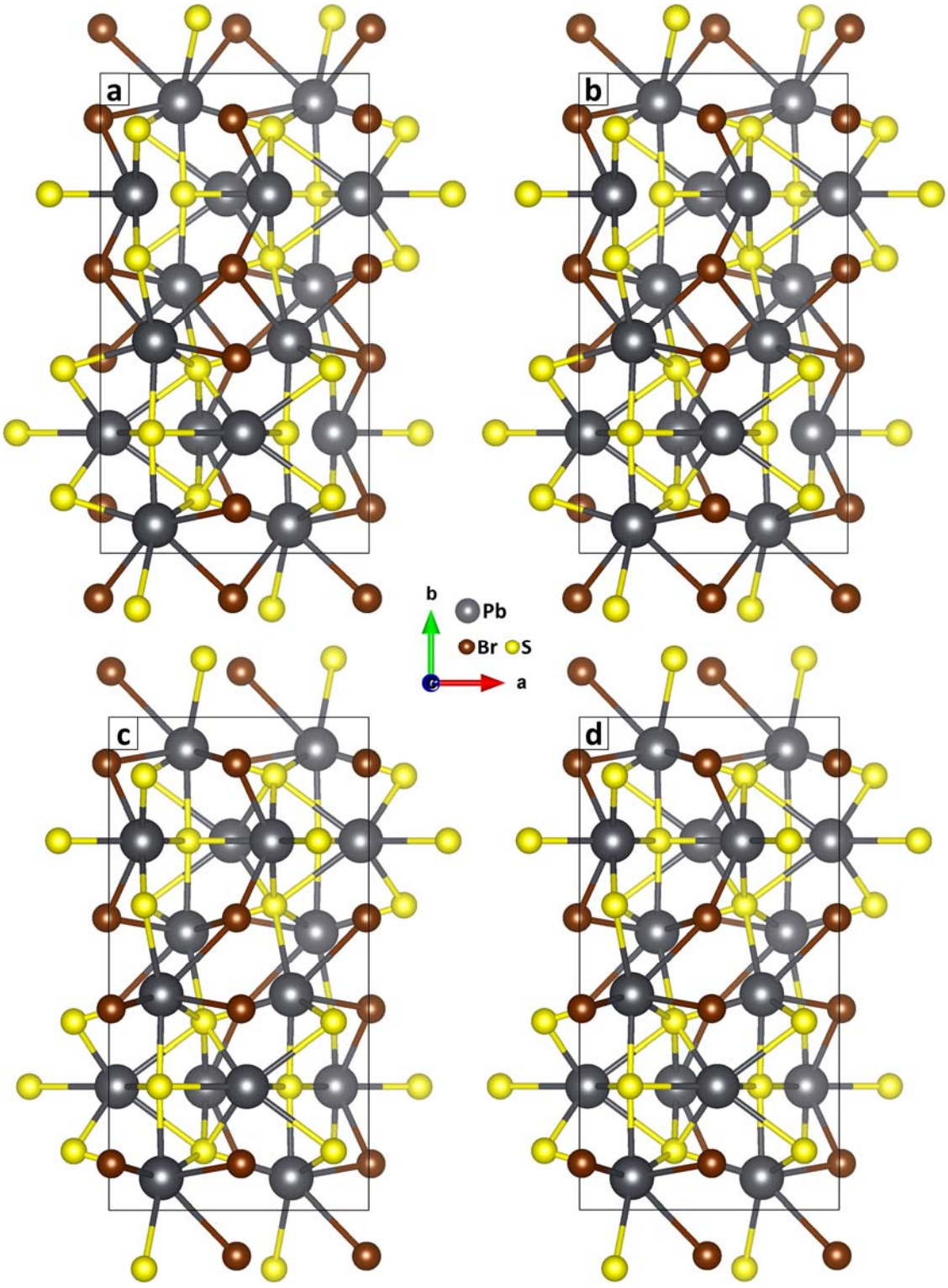

Figure S20. DFT-relaxed 3D-ED and XRPD based structures. Upper panels: structures emerging from DFT calculations by keeping the unit cell parameters fixed (for both a = 8.22592 Å, b = 14.70843, c = 8.13988 Å) and using the a) 3D-ED and b) XRPD based unit cells as input structures. The two models converged to the same structure, based on the level of calculation tolerances. Lower panels: structures emerging from DFT calculations by letting the unit cell parameters free to vary and using the c) 3D-ED and d) XRPD based unit cells as input structures. Again, the two models converged to the same structure, and remarkably the unit cell parameters converged to values compatible with those measured for nanoplatelets by 3D-ED (for both a = 8.14556 Å, b = 15.41923, c = 8.08130 Å).

j) Comparison between the proposed structures for $Pb_4S_3I_2$, $Pb_4S_3Br_2$ and $Pb_3S_2Cl_2$ NCs.

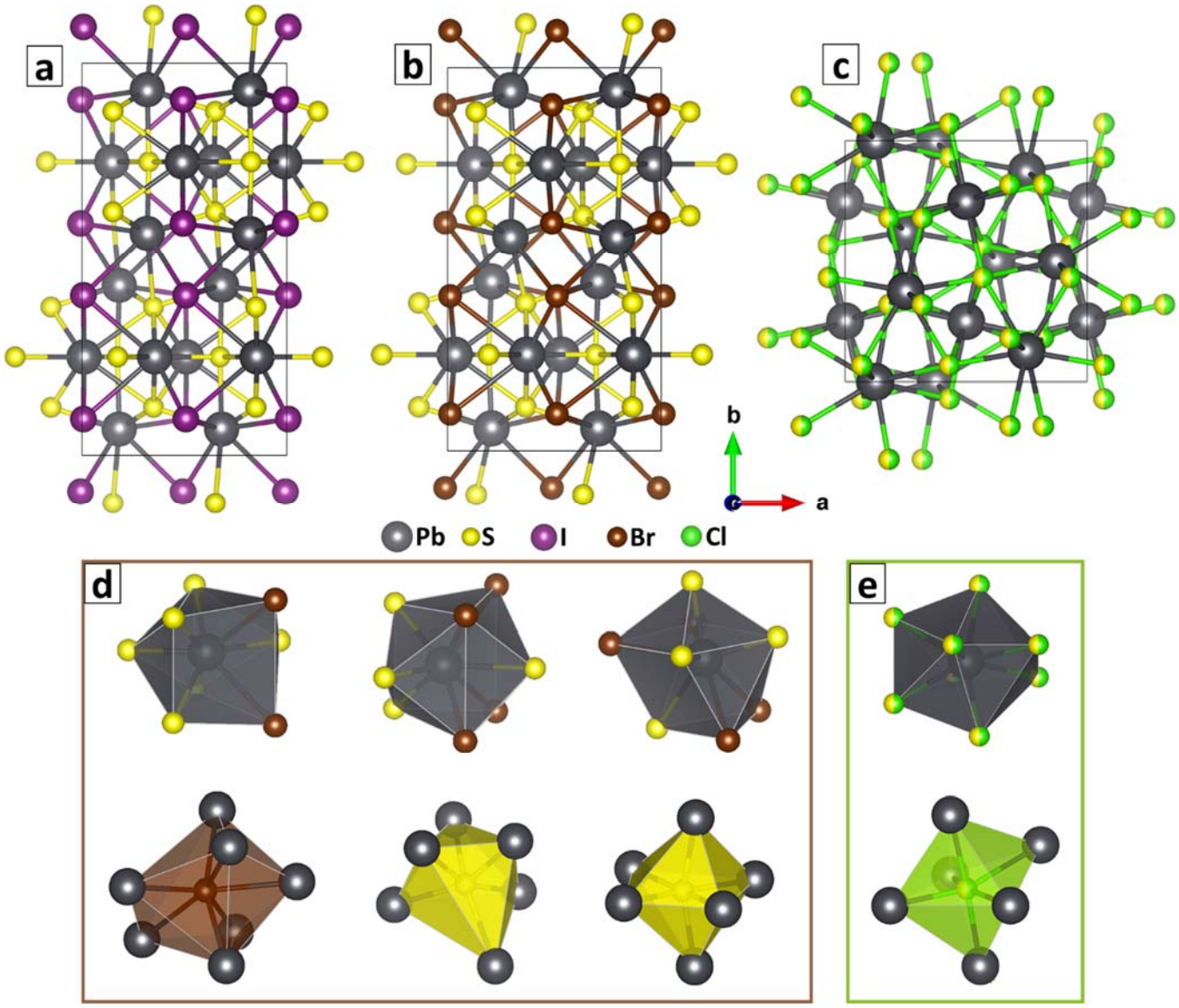

Figure S21. $Pb_4S_3I_2$, $Pb_4S_3Br_2$ and $Pb_3S_2Cl_2$ crystal structures and coordination polyhedra. The crystal structures proposed for NCs of $Pb_4S_3I_2$ (a), $Pb_4S_3Br_2$ (b) and $Pb_3S_2Cl_2$ (c). Iodide- and bromide-based NCs are clearly isostructural, while $Pb_3S_2Cl_2$ shows no resemblance to the other two structures at a first sight. However, the coordination polyhedra for all three structures are very similar.

k) Rietveld refinement of the $Pb_4S_3Br_2$ structure

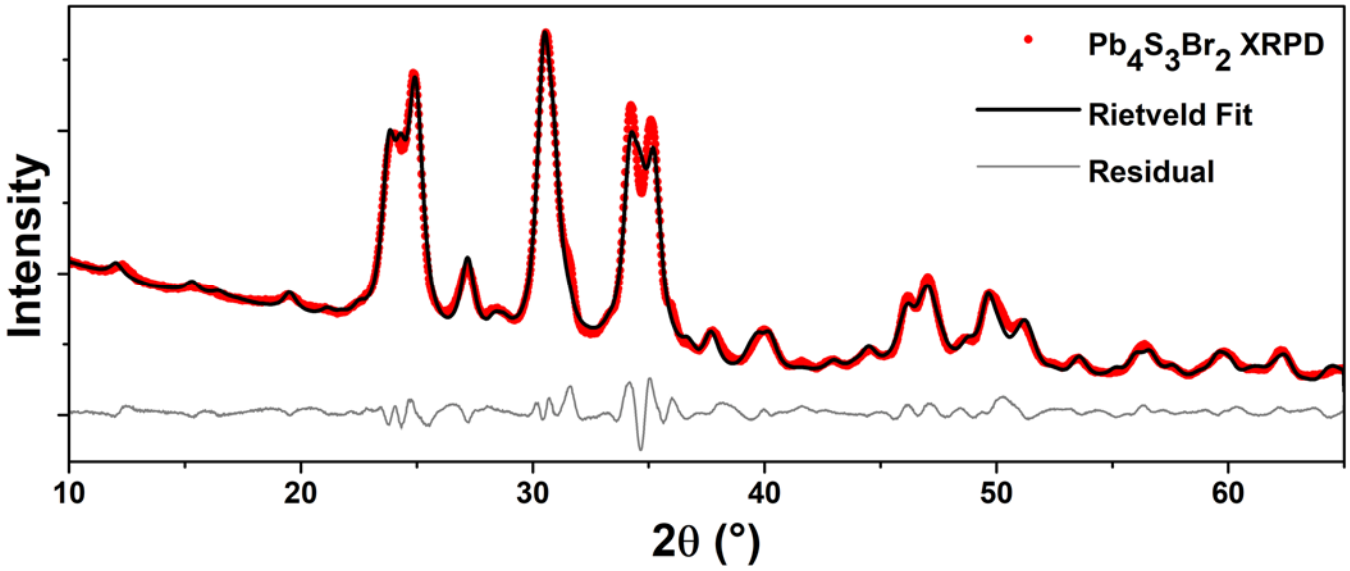

Figure S22. $Pb_4S_3Br_2$ XRPD. Rietveld refinement of the $Pb_4S_3Br_2$ NCs structural model shown in Figure 4d.

The Rietveld refinement of the structural model originally obtained from the DFT/PBE relaxation was performed by fitting an XRPD pattern measured on ~15 nm particles. The refined parameters were (listed according to the refinement order):

- Unit cell parameters
- Atomic coordinates
- Isotropic size parameter
- Anisotropic thermal factors (only positive or null parameters were accepted)
- Refinable-points linear interpolation background

The outcome of the refinement is summarized in the table below.

Table S8. $Pb_4S_3Br_2$ Rietveld Refinement. Outcome of the Rietveld refinement on the $Pb_4S_3Br_2$ structural model.

Space group	Pnma (no. 62)					
Unit cell parameters	**a (Å)**		**b (Å)**		**c (Å)**	
	8.202		14.707		8.165	
	α (°)		**β (°)**		**γ (°)**	
	90		90		90	
Atomic coordinates	**x**		**y**		**z**	
Pb 1	0.134		0.750		0.168	
Pb 2	0.464		0.750		0.810	
Pb 3	0.7918		0.944		0.985	
S 1	0.774		0.750		0.006	
S 2	0.673		0.871		0.619	
Br 1	0.477		0907		0.169	
Anisotropic Thermal Factors / Form Factors	**B11**	**B22**	**B33**	**B12**	**B13**	**B23**
Pb 1	0.02609	0.13468	0	0	0.02761	0
Pb 2	0.04174	0.09132	0.01543	0	0	0
Pb 3	0.12421	0.01533	0.12751	0.01001	0	0.02785
S 1	0	0	0	0	0	0
S 2	0.07355	0	0	0.04823	0	0.02516
Br 1	0.0652	0.03762	0	0	0.05184	0.04434
Goodness of Fit	8.3					

Notes on the fit: refining the anisotropic thermal factors was needed in order to reach a good match between the data and the calculated profile. Only null or positive values were allowed.

The following crystal structures are available to the reader in the form of .CIF files;

- DFT-relaxed structure as shown in Figure 4d: Pb4S3Br2_DFT.cif
- Rietveld-refined structure: Pb4S3Br2_Rietveld.cif

l) Band structures computed by DFT calculations

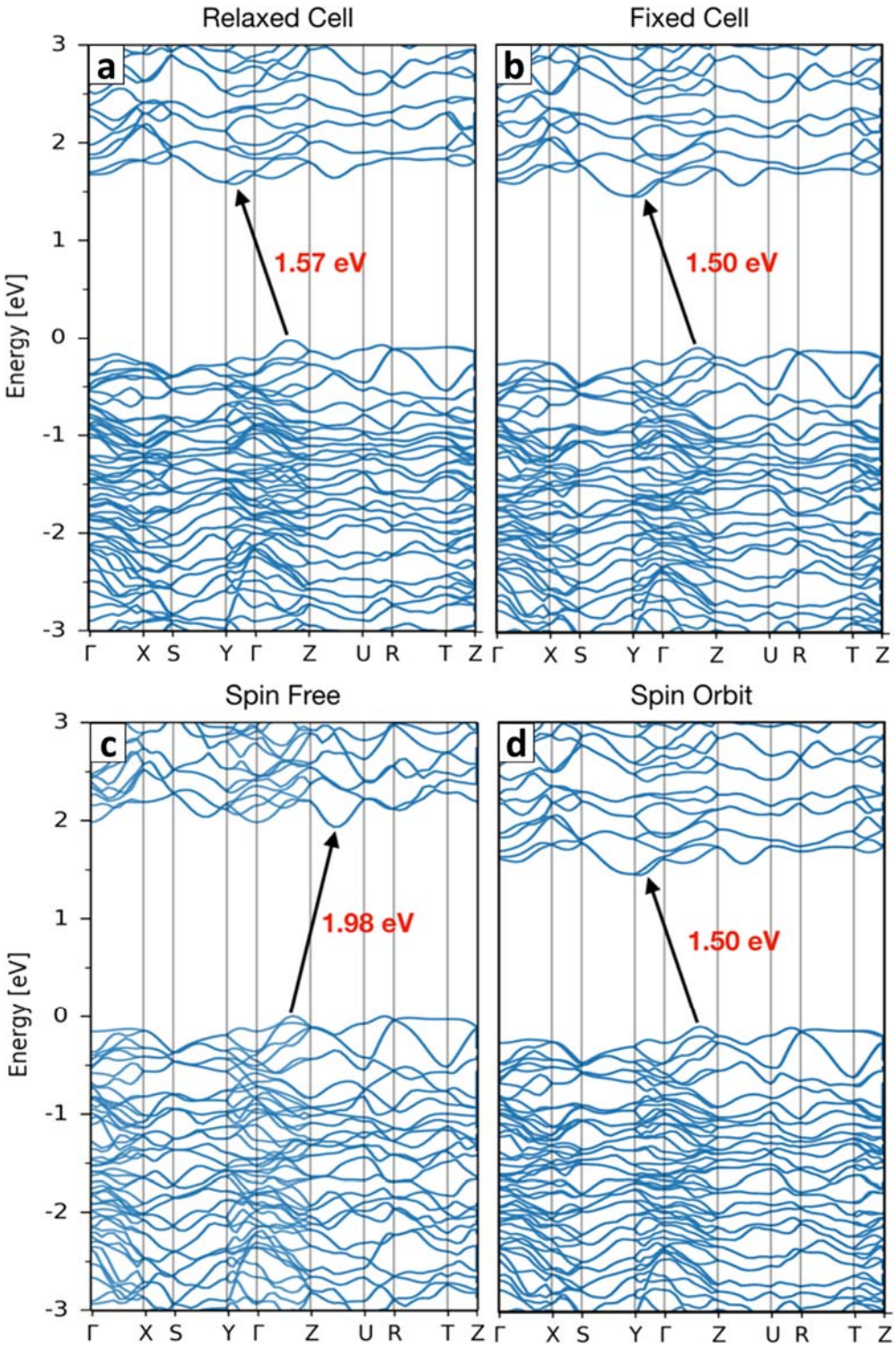

Figure S23. Calculated band structures for $Pb_4S_3Br_2$. Top**:** band structures computed on the unit cells with a) relaxed parameters (which converged to a = 8.14 Å, b = 15.42Å, c= 8.08 Å, corresponding to nanoplatelets, Figure S20c-d) and b) with fixed parameters (a = 8.226 Å, b = 14.708 Å, c = 8.140 Å, corresponding to pseudospherical NCs, Figure S20a-b). The composition of the band states remains similar, with only a slight widening of the gap from the constrained (fixed) to the unconstrained (relaxed) cell. Bottom: band structures of the fixed parameters unit cell computed c) excluding and d) including spin orbit coupling. In both cases the gap is indirect, however the spin free case shows a different k-point at the bottom of the conduction band; the band gap also increases up to about 2 eV. All band structures have been computed at the DFT/PBE level of theory.

m) Temporal stability assessment for $Pb_4S_3Br_2$ NCs

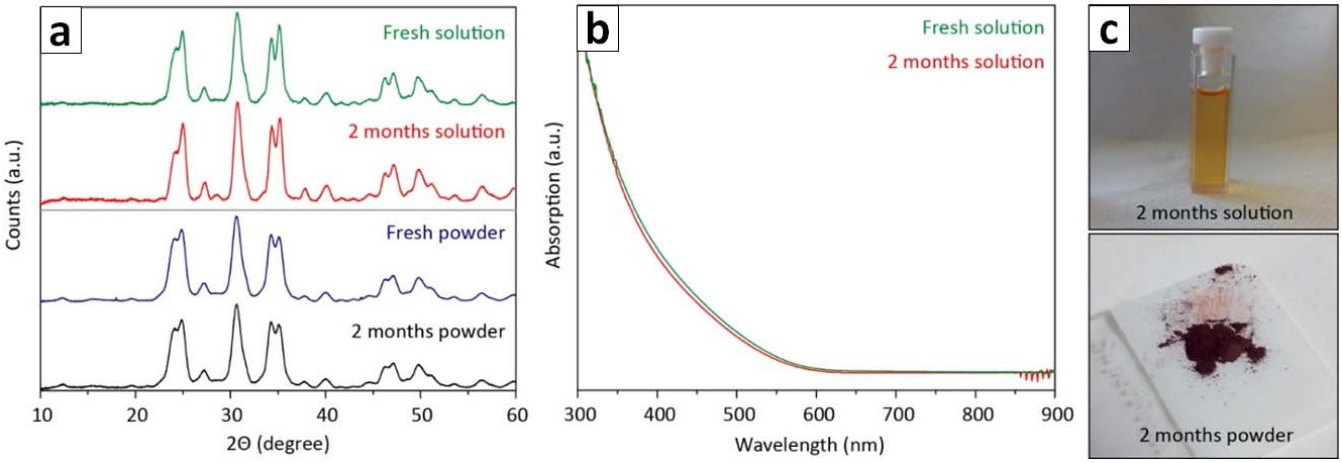

Figure S24. Temporal stability of $Pb_4S_3Br_2$ NCs. a) XRPD patterns of the same $Pb_4S_3Br_2$ NC colloidal suspension / dry powder as-prepared and after 2 months of aging in a dry and dark environment. b) Absorption spectra of the solution before and after aging. c) Photographs of the two samples after 2 months of aging. No differences are visible when compared with a freshly prepared sample.

n) FTIR characterization of $Pb_4S_3Br_2$ NCs and devices.

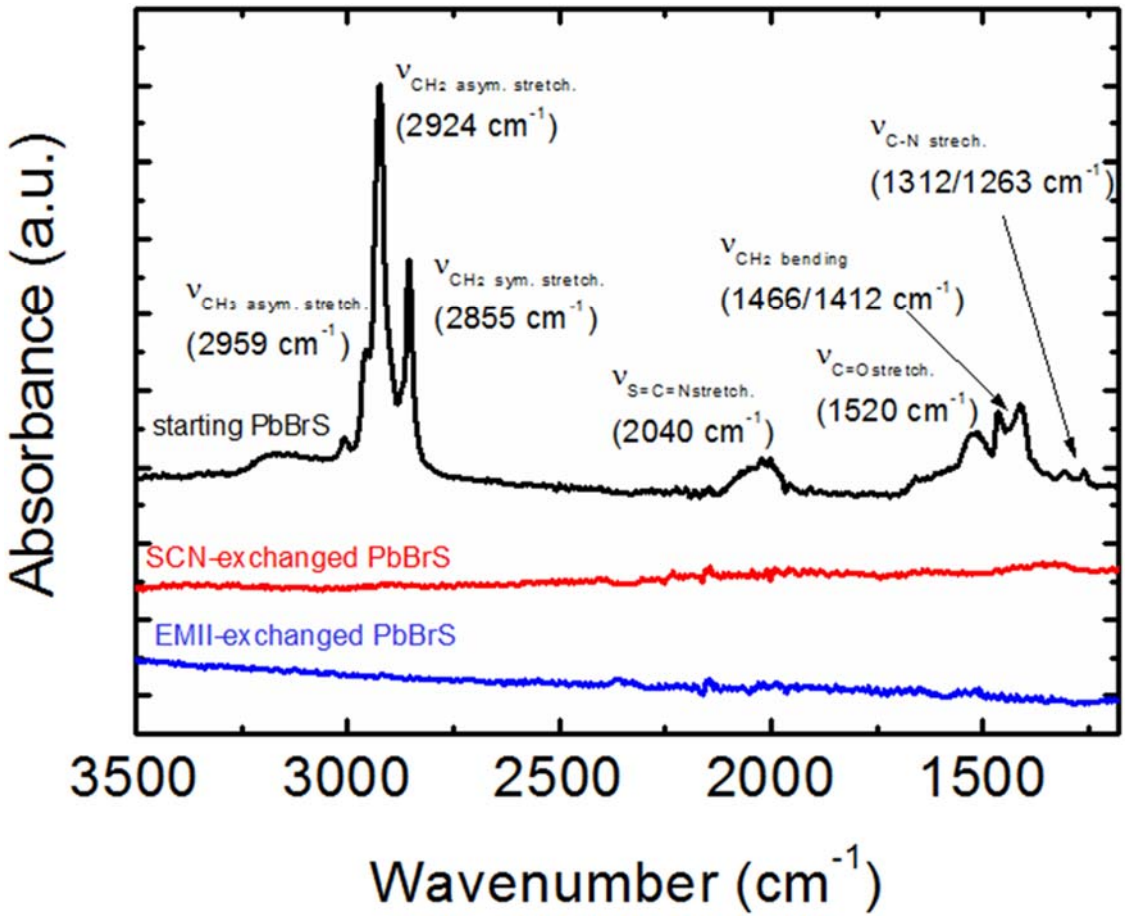

Figure S25. FTIR characterization of films of $Pb_4S_3Br_2$ NCs before and after ligand exchange. FTIR spectra of the as-synthesized $Pb_4S_3Br_2$ NCs, showing the characteristic signal of organic ligands (*black*) compared with that of NCs after being exchanged with SCN and EMII (*red, blue*). After the treatments, the original organic ligands have been quantitatively removed.

o) XPS and UPS analyses ligand-exchanged $Pb_4S_3Br_2$ NCs for devices.

As reported in the main text, to make a film of $Pb_4S_3Br_2$ NCs conductive and use it as active layer in a photovoltaic device, we performed a solid-ligand exchange with 1-ethyl-3-methylimidazolium iodide (EMII, see details in the main manuscript). The effectiveness of the ligand replacement as well as the suitability of the energy level alignment from the ligand exchange in the layered stack were investigated via XPS and UPS. Figure S26 shows the comparison of the wide scans collected on the pristine sample and on the sample after ligand exchange. The surface of the starting sample contained carbon and oxygen species due to the original organic ligands used in the colloidal synthesis (see O 1s and C 1s peaks at approx. 530 eV and 285 eV, respectively, in the wide scan shown in the top panel of Figure S8). After ligand exchange, the intensity of those signals was strongly reduced, indicating the effective removal of the ligands; at the same time, signals due to the presence of iodine appeared. The position of the main I 3d peak at (619.5 ± 0.2) eV indicates that iodine is present as iodide, in agreement with literature,[3] and further corroborating the effectiveness of the ligand exchange procedure.

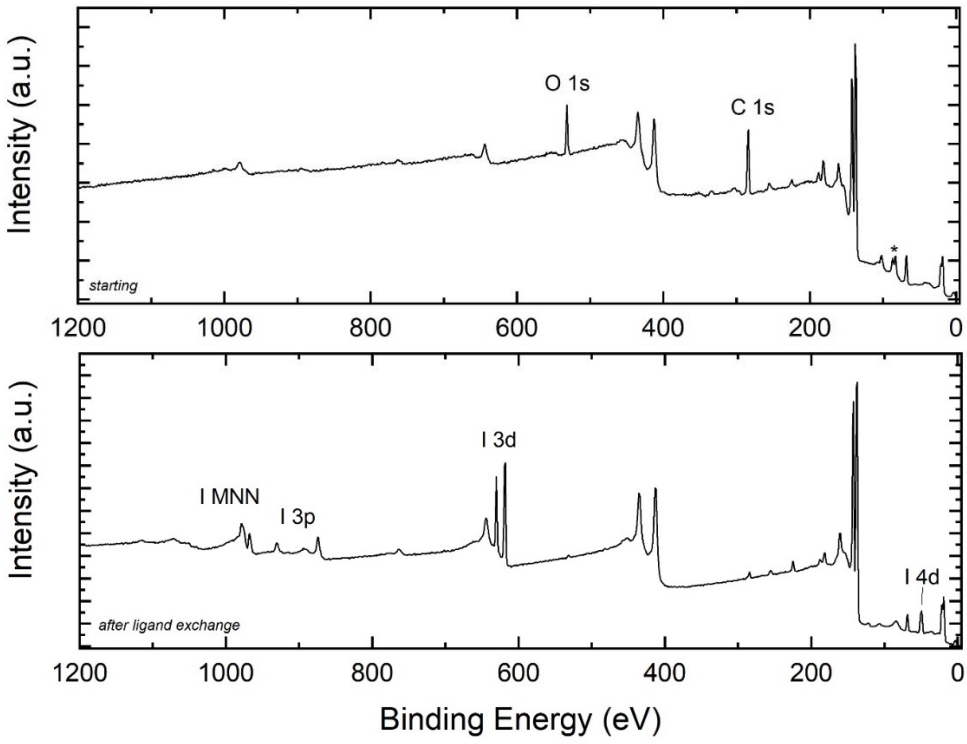

Figure S26. XPS analysis on ligand-exchanged $Pb_4S_3Br_2$ NCs for solar cell tests. XPS data collected on as synthesized $Pb_4S_3Br_2$ NCs (top panel) and on those after the ligand exchange (bottom panel). The ligand exchange induced a drastic reduction of the surface carbon and oxygen species, as evidenced by the decrease of the intensities of the O 1s and C 1s peaks, confirming the effective removal of the starting ligands. At the same time, signals due to iodine species appeared, due to the surface passivation with iodide ions of EMII. Note: in the top panel, at approx. 84 eV, the signals due to the gold substrate are visible.

We further studied the ligand-exchanged sample *via* UPS, to extract its work function and the valence band maximum (VBM) position. The results are reported in Figure S27, together with the linear extrapolation of the high and low binding energy onsets. The high binding energy onset is directly correlated with the work function (WF) of the material. With the measured onset at 16.9 eV, we calculated the WF as difference between the He I photon energy and the onset value itself. The resulting WF is 4.30 ± 0.05 eV. The low binding energy onset relates instead with the distance between the top of the valence band (VBM) and the Fermi level (E_F), assumed as zero of the binding energy scale. As shown in the figure, the position of the valence band maximum is at 1.6 ± 0.1 eV below E_F. The position of VBM with respect to the vacuum level is therefore -5.9 ± 0.12 eV.

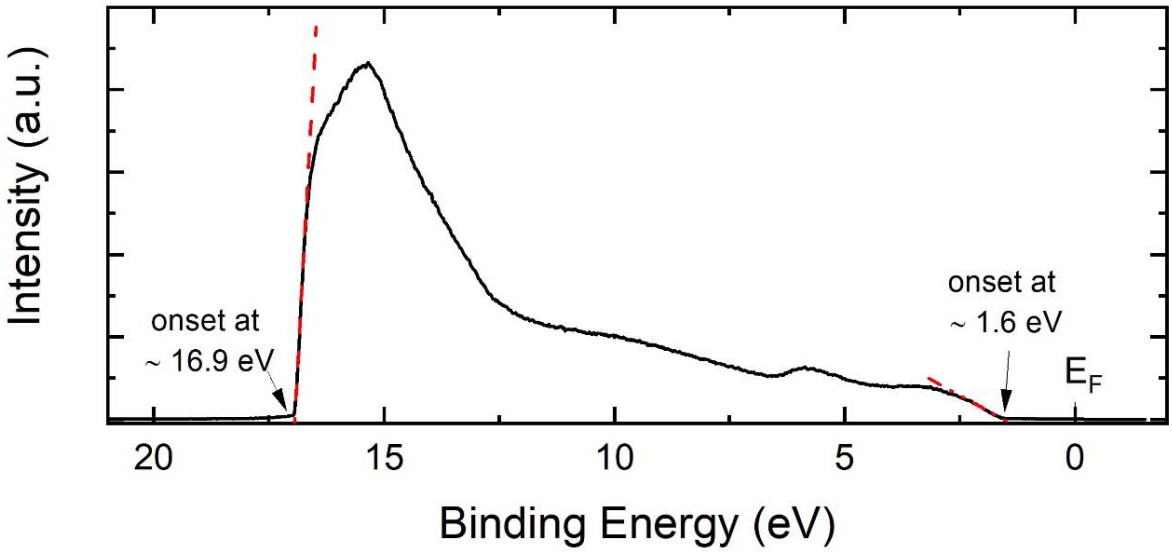

Figure S27. UPS analysis on ligand-exchanged $Pb_4S_3Br_2$ NCs for solar cell tests. UPS data collected on the $Pb_4S_3Br_2$ nanocrystals after the ligand exchange procedure. The high and low binding energy onsets, as obtained via linear extrapolation, are marked.

As a further evidence of the possibility to tune the energy levels of the $Pb_4S_3Br_2$ NCs, we also carried out UPS analysis of the sample that had been ligand-exchanged with NH_4SCN and used for the fabrication of the photodetectors (see procedure in the main text). The results are reported in Figure S28, together with the data collected on starting organic capped-NCs. Similarly to what done on the sample that had been ligand-exchanged with EMII, we obtained the WF and VBM position on these two samples via linear extrapolation of high and low binding energy onsets. For the pristine sample, before ligand exchange, the resulting WF is 4.10 ± 0.05 eV and the VBM is at 1.1 ± 0.1 eV below E_F. The position of VBM with respect to the vacuum level is therefore -5.20 ± 0.11 eV. In the case of the SCN-exchanged sample, instead, the WF is 4.60 ± 0.05 eV and the VBM is at 0.9 ± 0.1 eV below E_F, corresponding to a

position with respect to the vacuum level of -5.20 ± 0.11 eV. These data therefore confirm that, as reported in literature for other colloidal NCs,[15,16] the energy levels of our $Pb_4S_3Br_2$ NCs could be tuned by a proper choice of the surface ligands.

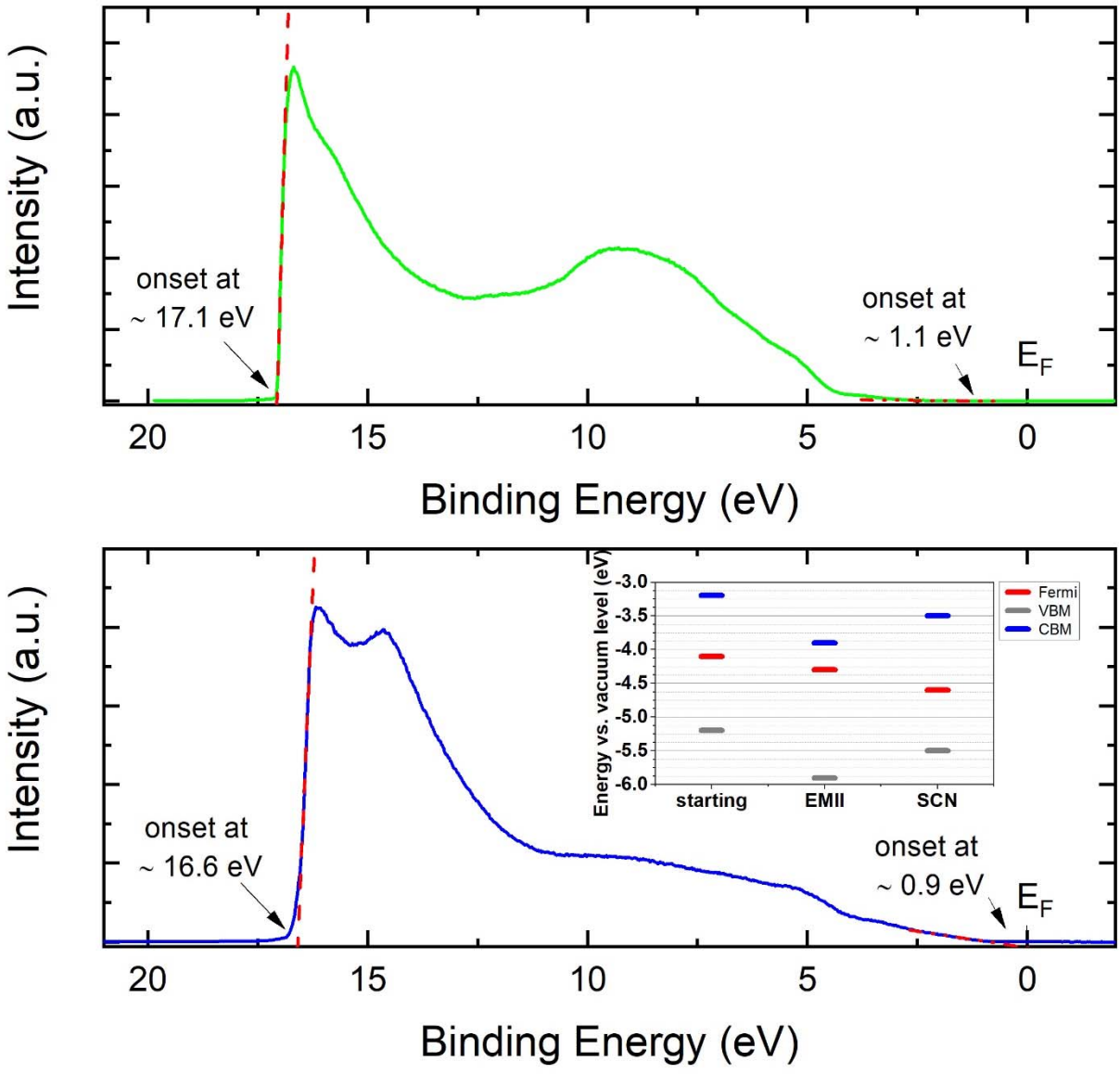

Figure S28. UPS analysis on starting and SCN- ligand-exchanged $Pb_4S_3Br_2$ NCs. UPS data collected on the $Pb_4S_3Br_2$ NCs before (top) and after the ligand exchange procedure with NH_4SCN (bottom). The high and low binding energy onsets, as obtained via linear extrapolation, are marked. Inset in bottom panel shows the energy level diagrams of the $Pb_4S_3Br_2$ NCs with the ligands used in this work. The position of the conduction band minimum (CBM) has been obtained by adding the optical bandgap (approx. 2 eV) to the position of the VBM.

p) Complementary characterization for the photodetectors and solar cells.

Figure S29 shows the Noise Power Spectrum Density of a time trace acquired from the photodetector in the dark, in the same experimental condition of the light response measurements (Fig. 6a-c of the main text). From this spectrum, the noise figures of merit were calculated.

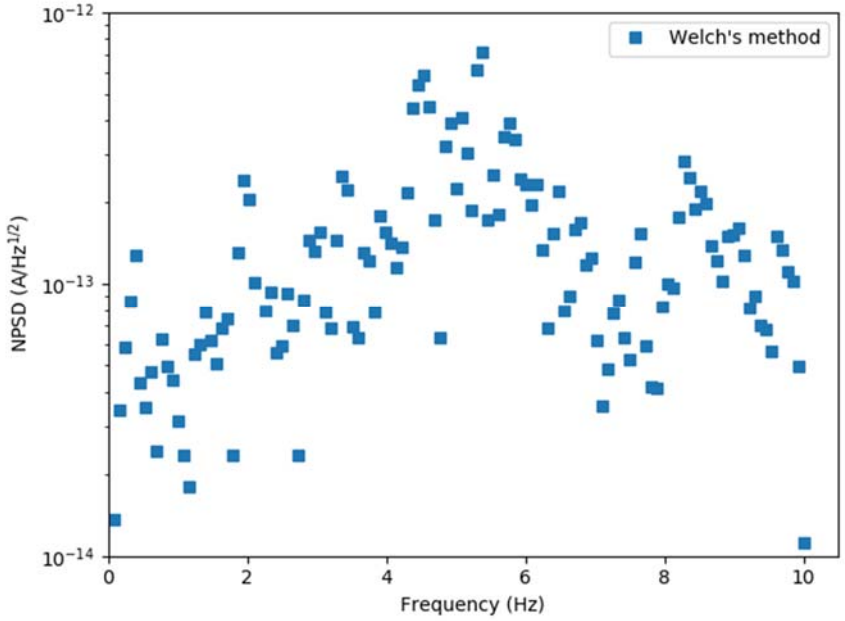

Figure S29. Noise Power Spectrum Density calculated from the Fourier Transform (using the Welch's method)[14], of a time trace in the dark, after removing a constant background.

Figure S30a shows the I-V characteristics in dark and light of the photodetector made from SCN-exchanged $Pb_4S_3Br_2$ NC film. Regarding the solar cell, Figure S30b-c show a representative SEM image of the film together with the stability tests of the cell carried out during storage in air and dark conditions (data averaged from 3 different devices).

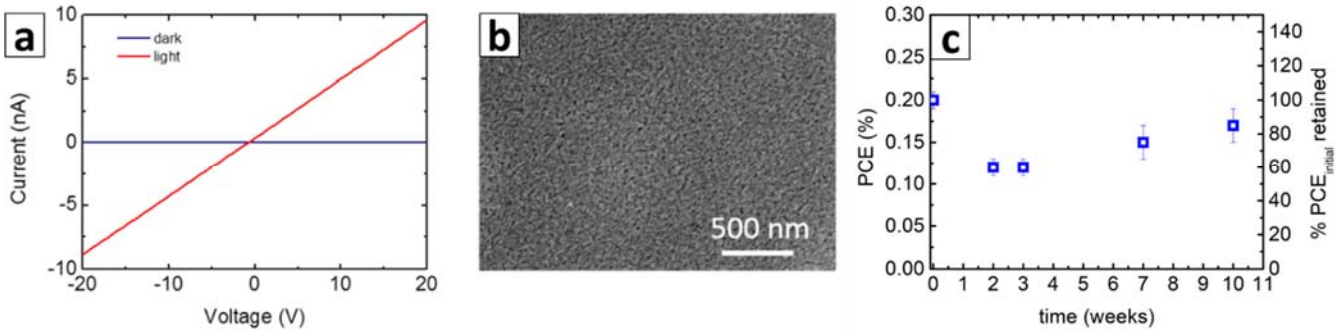

Figure S30. Complementary characterization for the photodetectors and solar cells. a) I–V characteristics of the $Pb_4S_3Br_2$ NC-based photodetector with Ti/Au interdigitated bottom contacts (gap of 1μm) in dark and under white LED light (400−750nm, 100 mW cm^{-2}). b) Representative SEM image of the $Pb_4S_3Br_2$ NC film used in the solar cell stack. c) Time evolution of the PCE of the solar cells stored in the dark under ambient conditions. Values shown are the average results from the monitoring of 3 different devices.

q) Direct synthesis and structural characterization of $Pb_4S_3I_2$ NCs

Conditions similar to those described in paragraph S1.a were applied for the synthesis of $Pb_4S_3I_2$ NCs: 0.2 mmol of PbI_2 and 0.2 mmol of $Pb(SCN)_2$ were dissolved in a mixture of 10 mL ODE and 250 µL of OLAM and OA at 110°C in a 25 mL three-necked flask. The rest of the procedure remained unchanged. It is noteworthy that the dissolution of PbI_2 was faster than that of $PbBr_2$ and led to an intensely colored yellow solution. NCs formed upon heating up were generally larger than those of $Pb_4S_3Br_2$ (if compared at the same quench temperature, *e.g.* 180°C) and following the centrifugation they were completely recovered, leaving an almost colorless precipitate. The heat-up process causes the NCs to form, even if with the presence of a crystalline impurity which we identified as PbI_2 nanosheets or flakes based on reports in the literature.[2,17]

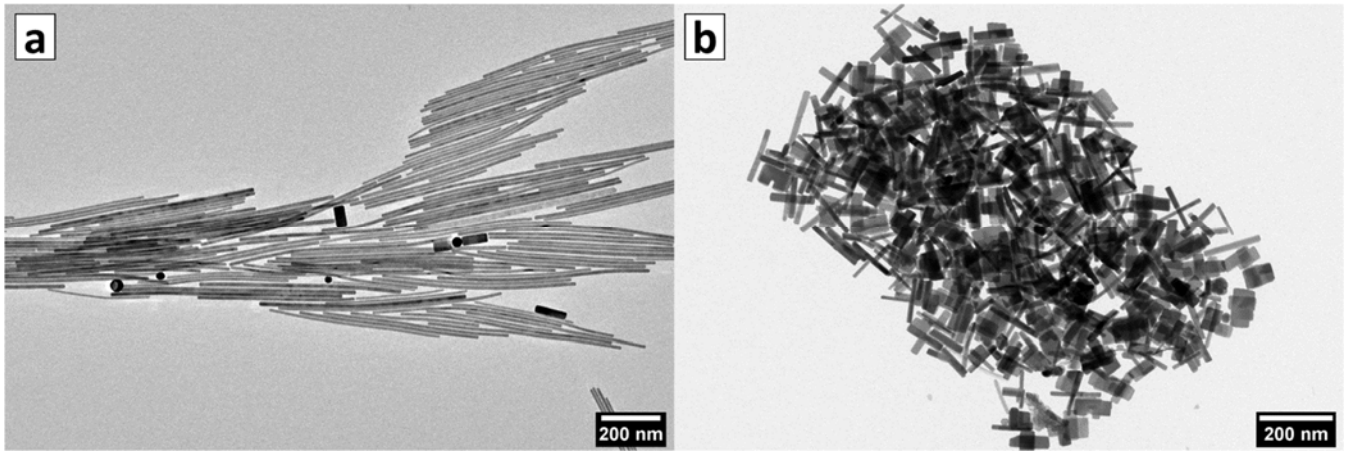

Figure S31. $Pb_4S_3I_2$ NCs. Two of the morphologies obtained for $Pb_4S_3I_2$ nanostructures. Even if the shape and size control was poor, the $Pb_4S_3I_2$ NCs appeared to grow in more anisotropic shapes and to reach larger sizes compared to the $Pb_4S_3Br_2$ NCs.

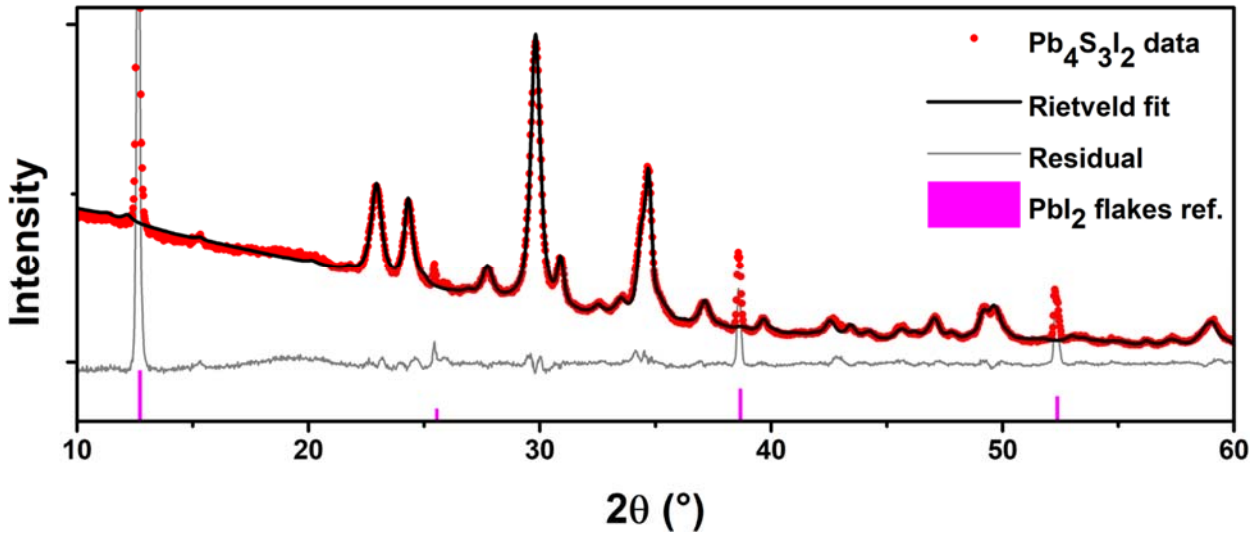

Figure S32. $Pb_4S_3I_2$ XRPD. Rietveld fit of the $Pb_4S_3I_2$ NCs XRPD pattern based on the structural model published by Ni *et. al*.[18] The good fit of the overall profile confirms that we obtained the expected phase, but evidences the presence of a crystalline impurity in non-negligible amounts, clearly indicated by the peaks found in the residual profile. A good match with the pattern of PbI_2 flakes is observed.[2]

Table S9. $Pb_4S_3I_2$ Rietveld fit. Outcome of the Rietveld fit based on the $Pb_4S_3I_2$ structural model published by Ni *et. al.*[18]

Space group	Pnma (no. 62)					
Unit cell parameters	**a (Å)**		**b (Å)**		**c (Å)**	
	8.169		15.648		8.201	
	α (°)		**β (°)**		**γ (°)**	
	90		90		90	
Atomic coordinates	**x**		**y**		**z**	
Pb 1	0.18269		0.06747		0.07378	
Pb 2	0.00957		0.250		0.31804	
Pb 3	0.34420		0.250		0.60805	
S 1	0.33767		0.11501		0.35901	
S 2	0.20698		0.25000		-0.00224	
I 1	0.00909		0.08462		0.65668	
Isotropic Thermal Factors	**B**					
Pb 1	8.67037					
Pb 2	4.40629					
Pb 3	5.75456					
S 1	4.19821					
S 2	0					
I 1	5.34747					
Anisotropic Lorentzian size broadening factors	Y00	Y20	Y22+	Y40	Y42+	Y44+
	5.78980	0.28502	-1.87900	0.31184	-0.79490	-1.95033
Goodness of Fit	9.9					

Note on the fit: the anisotropic broadening factors were included in order to take into account the anisotropic shape observed in NCs under the electron microscope. The relatively high Goodness of Fit parameter (lower is better) depends mainly on the presence of the non-fitted impurity peaks.

r) Direct synthesis and structural characterization of $Pb_3S_2Cl_2$ NCs

Conditions similar to those described in paragraph S1.a were applied for the synthesis of $Pb_3S_2Cl_2$ NCs: 0.2 mmol of PbI_2 and 0.2 mmol of $Pb(SCN)_2$ were dissolved in a mixture of 10 mL ODE and 250 µL of OLAM and OA at 110°C in a 25 mL three-necked flask. The dissolution of $PbCl_2$ was slower than that of $PbBr_2$ and sometimes was incomplete. Thus, we introduced an additional filtering step: we let the batch cool down to ~50°C, decanted it for a few seconds and then filtered the liquid with a 0.2 µm PTFE syringe filter. The clear liquid was then heated up again to 110°C and the procedure continued unchanged. NCs formed upon heating up were generally smaller than those of $Pb_4S_3Br_2$ (if compared at the same quench temperature, *e.g.* 170°C) and were recovered via ethyl-acetate assisted precipitation. One advantage of this approach is that we also eliminated the large PbS NCs that often formed during the synthesis and that were found in the precipitate.

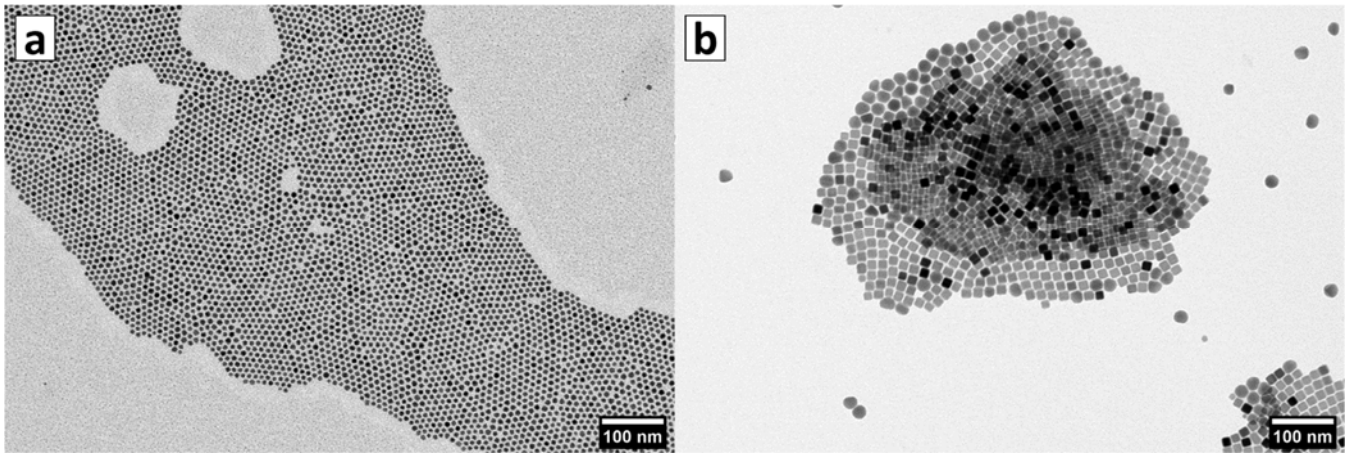

Figure S33. $Pb_3S_2Cl_2$ NCs. a) Smaller $Pb_3S_2Cl_2$ NCs obtained by quenching the reaction at 170°C and recovering the supernatant via ethyl-acetate assisted precipitation and b) rounded $Pb_3S_2Cl_2$ NCs found in the precipitate and heavily contaminated by cubic PbS NCs (both are visible in the image).

Differently from the case of $Pb_4S_3I_2$, no ternary Pb-S-Cl phases matching with our material could be found in crystal structure databases (COD, ICSD). However, an unexpected help in its identification came from the work of Rabenau *et. al.* (dated 1969), in which they reported two tentative new phases, named "2PbS + $PbBr_2$" and "2PbS + $PbCl_2$".[19] According to their report, the first phase was obtained pure in form of a precipitate by first dissolving PbS in concentrated HBr and subsequently diluting the solution with water. They measured its stoichiometry and collected the XRPD pattern but could not solve the structure. The second phase was obtained via a similar protocol, involving HCl instead of HBr, and produced a red precipitate which rapidly decomposed to form a black powder. Thus, they could not collect it pure; however, they measured the XRPD of the mixture, finding that it was mainly composed by PbS but also contained a residual which produced a pattern similar to that of "2PbS + $PbBr_2$". Hence, they hypothesized

the existence of a "2PbS + $PbCl_2$" phase. Sixty-one years later, Ni *et. al.* reported the solid-state synthesis of the high-pressure chalcohalide $Pb_3Se_2Br_2$ (4 GPa, 700°C), which features an equivalent stoichiometry and a pattern very close to that of our chlorine-based NCs[20] (after proper shifting of the peaks to take into account the different sizes of the cells). Figure S34 compares the XRPD we measured that reported for "2PbS + $PbCl_2$" and for $Pb_3Se_2Br_2$, suggesting that we obtained NCs of the $Pb_3S_2Cl_2$ phase that Rabenau *et. al.* hypothesized many years ago.

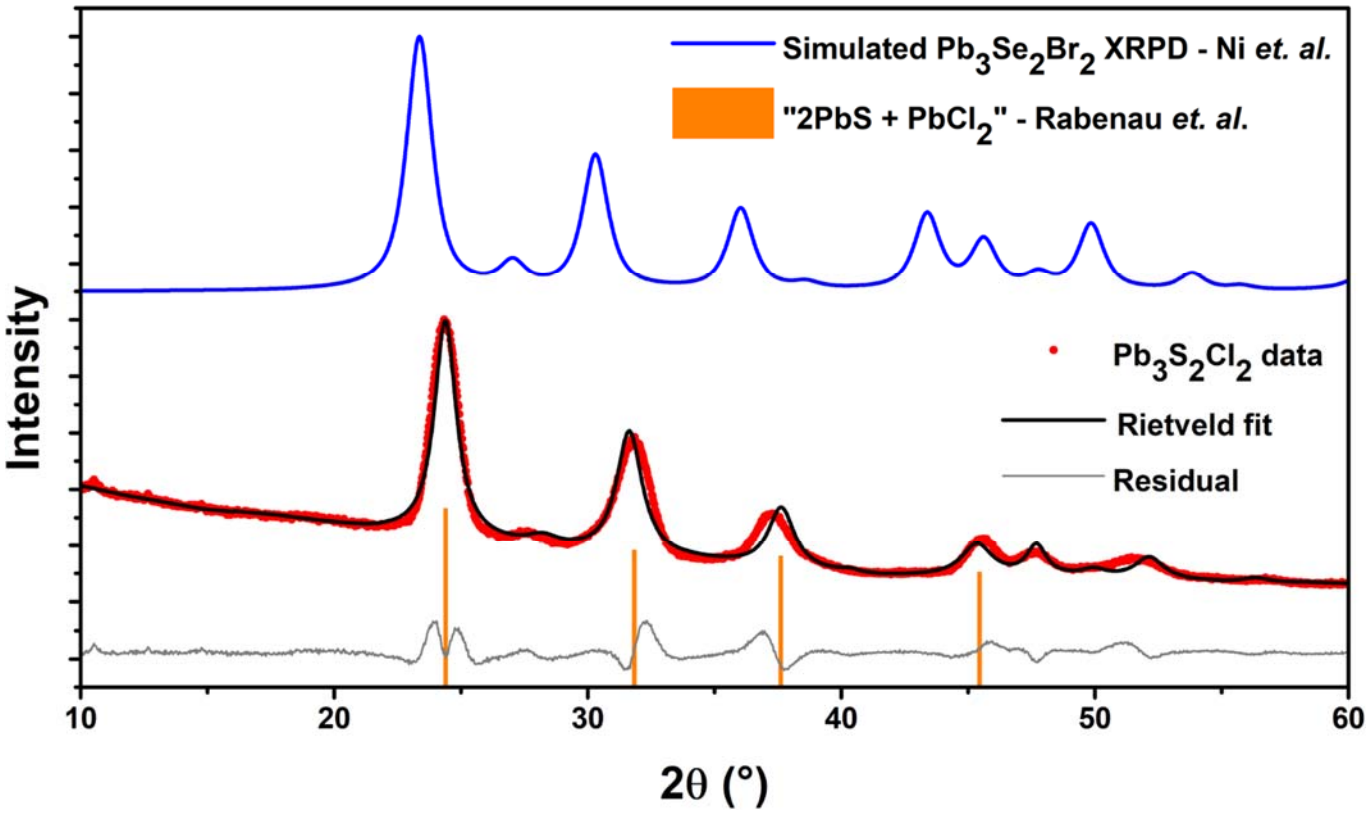

Figure S34. $Pb_3S_2Cl_2$ XRPD. XRPD data from $Pb_3S_2Cl_2$ NCs and corresponding Rietveld fit based on the structural model published by Ni *et.al.*[20] for the phase $Pb_3Se_2Br_2$ The simulated XRPD pattern for the latter and the XRPD lines reported by Rabenau *et.al* for the hypothesized "2PbS + $PbCl_2$" phase are shown for comparison.

Note on the fit: only the unit cell parameters and the scale factor were refined. All the remaining parameters were kept as originally determined by Ni *et.al.* in their work.[20] The overall fit match is good, but the residual indicates that the peaks are slightly misplaced. The cause is most likely a slight distortion from the original cubic symmetry. However, due to the peak broadening the information needed to address this deformation was lost, and we preferred to keep a pseudocubic description for the structure. We plan to investigate this aspect in further specific studies.

Table S10. $Pb_3S_2Cl_2$ Rietveld fit. Outcome of the Rietveld fit on the $Pb_3S_2Cl_2$ XRPD obtained by adapting the $Pb_3Se_2Br_2$ structural model published by Ni. *et. al.*[20]

Space group	Pnma (no. 62)		
Unit cell parameters	**a (Å)**	**b (Å)**	**c (Å)**
	8.202	14.707	8.165
	α (°)	**β (°)**	**γ (°)**
	90	90	90
Goodness of Fit	8.3		

s) DFT band structure calculations for $Pb_4S_3I_2$ and $Pb_3S_2Cl_2$

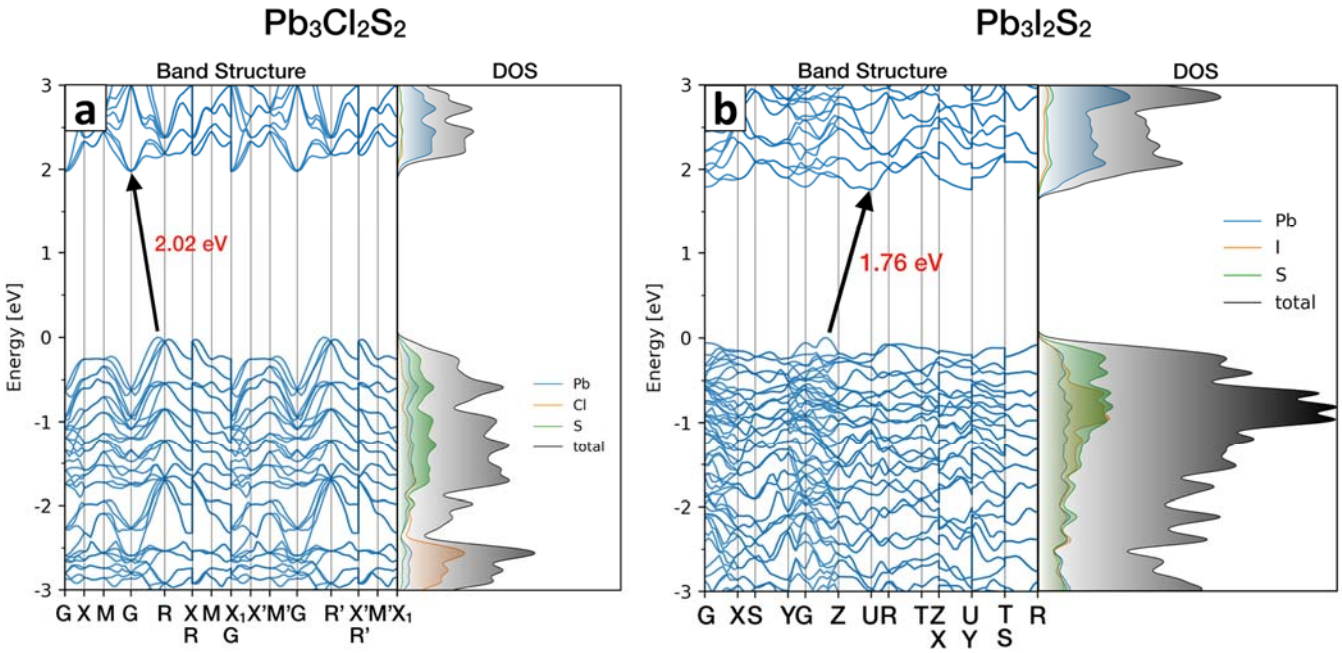

Figure S35. Calculated band structures for $Pb_3S_2Cl_2$ and $Pb_4S_3I_2$, based on the structures published by Ni *et. al.* [18,20] The calculations were performed starting from the models obtained by Rietveld fit as reported in sections S.q and S.r, after relaxing the unit cell content while keeping the cell parameters fixed. Since Cl and S atoms in $Pb_3S_2Cl_2$ share randomly the same Wyckoff sites, a stoichiometric cell with random distribution of the two elements was considered. Calculations were performed without including spin orbit coupling (SOC) to better estimate the bandgap.

References

(1) Akkerman, Q. A.; García, B. M.; Buha, J.; Almeida, G.; Toso, S.; Marras, S.; Bonaccorso, F.; Petralanda, U.; Infante, I.; Manna, L. Ultrathin Orthorhombic PbS Nanosheets. *Chem. Mater.* **2019**. https://doi.org/10.1021/acs.chemmater.9b02914.

(2) Lin, D. Y.; Guo, B. C.; Dai, Z. Y.; Lin, C. F.; Hsu, H. P. Pbi2 Single Crystal Growth and Its Optical Property Study. *Crystals* **2019**, *9* (11), 589. https://doi.org/10.3390/cryst9110589.

(3) NIST X-ray Photoelectron Spectroscopy (XPS) Database, Version 4.1 https://srdata.nist.gov/xps/.

(4) Altomare, A.; Cuocci, C.; Giacovazzo, C.; Moliterni, A.; Rizzi, R.; Corriero, N.; Falcicchio, A. EXPO2013: A Kit of Tools for Phasing Crystal Structures from Powder Data. *J. Appl. Crystallogr.* **2013**, *46* (4), 1231–1235. https://doi.org/10.1107/S0021889813013113.

(5) Altomare, A.; Campi, G.; Cuocci, C.; Eriksson, L.; Giacovazzo, C.; Moliterni, A.; Rizzi, R.; Werner, P. E. Advances in Powder Diffraction Pattern Indexing: N-TREOR09. *J. Appl. Crystallogr.* **2009**, *42* (5), 768–775. https://doi.org/10.1107/S0021889809025503.

(6) de Wolff, P. M. A Simplified Criterion for the Reliability of a Powder Pattern Indexing. *J. Appl. Crystallogr.* **1968**, *1* (2), 108–113. https://doi.org/10.1107/s002188986800508x.

(7) Altomare, A.; Caliandro, R.; Camalli, M.; Cuocci, C.; Da Silva, I.; Giacovazzo, C.; Moliterni, A. G. G, A. G.; Spagna, R. Space-Group Determination from Powder Diffraction Data: A Probabilistic Approach. *J. Appl. Crystallogr.* **2004**, *37* (6), 957–966. https://doi.org/10.1107/S0021889804023982.

(8) Altomare, A.; Camalli, M.; Cuocci, C.; Da Silva, I.; Giacovazzo, C.; Moliterni, A. G. G.; Rizzi, R. Space Group Determination: Improvements in EXPO2004. *J. Appl. Crystallogr.* **2005**, *38* (5), 760–767. https://doi.org/10.1107/S0021889805020820.

(9) Altomare, A.; Camalli, M.; Cuocci, C.; Giacovazzo, C.; Moliterni, A. G. G.; Rizzi, R. Advances in Space-Group Determination from Powder Diffraction Data. *J. Appl. Crystallogr.* **2007**, *40* (4), 743–748. https://doi.org/10.1107/S0021889807027501.

(10) Le Bail, A.; Duroy, H.; Fourquet, J. L. Ab-Initio Structure Determination of LiSbWO6 by X-Ray Powder Diffraction. *Mater. Res. Bull.* **1988**, *23* (3), 447–452. https://doi.org/10.1016/0025-5408(88)90019-0.

(11) Altomare, A.; Carrozzini, B.; Giacovazzo, C.; Guagliardi, A.; Moliterni, A. G. G.; Rizzi, R. Solving Crystal Structures from Powder Data. I. The Role of the Prior Information in the Two-Stage Method. *J. Appl. Crystallogr.* **1996**, *29 PART 6* (6), 667–673. https://doi.org/10.1107/s0021889896007467.

(12) Altomare, A.; Foadi, J.; Giacovazzo, C.; Moliterni, A. G. G.; Burla, M. C.; Polidori, G. Solving Crystal Structures from Powder Data. IV. The Use of Patterson Information for Estimating the |F|'s. *J. Appl. Crystallogr.* **1998**, *31* (1), 74–77. https://doi.org/10.1107/S002188989700945X.

(13) Altomare, A.; Cuocci, C.; Giacovazzo, C.; Moliterni, A. G. G, A. G.; Rizzi, R. Powder Diffraction: The New Automatic Least-Squares Fourier Recycling Procedure in EXPO2005. *J. Appl. Crystallogr.* **2006**, *39* (4), 558–562. https://doi.org/10.1107/S0021889806017912.

(14) Welch, P. D. The Use of Fast Fourier Transform for the Estimation of Power Spectra: A Method Based on Time Averaging Over Short, Modified Periodograms. *IEEE Trans. Audio Electroacoust.* **1967**, *15* (2), 70–73. https://doi.org/10.1109/TAU.1967.1161901.

(15) Brown, P. R.; Kim, D.; Lunt, R. R.; Zhao, N.; Bawendi, M. G.; Grossman, J. C.; Bulović, V. Energy Level Modification in Lead Sulfide Quantum Dot Thin Films through Ligand Exchange. *ACS Nano* **2014**, *8* (6), 5863–5872. https://doi.org/10.1021/nn500897c.

(16) Rastogi, P.; Palazon, F.; Prato, M.; Di Stasio, F.; Krahne, R. Enhancing the Performance of CdSe/CdS Dot-in-Rod Light-Emitting Diodes via Surface Ligand Modification. *ACS Appl. Mater. Interfaces* **2018**, *10* (6), 5665–5672. https://doi.org/10.1021/acsami.7b18780.

(17) Wang, R.; Li, S.; Wang, P.; Xiu, J.; Wei, G.; Sun, M.; Li, Z.; Liu, Y.; Zhong, M. PbI2 Nanosheets

for Photodetectors via the Facile Cooling Thermal Supersaturation Solution Method. *J. Phys. Chem. C* **2019**, *123* (14), 9609–9616. https://doi.org/10.1021/acs.jpcc.9b01322.

(18) Ni, D.; Guo, S.; Yang, Z. S.; Powderly, K. M.; Cava, R. J. $Pb_4S_3I_2$ –A High-Pressure Phase in the PbS-PbI 2 System. *Solid State Sci.* **2019**, *91*, 49–53. https://doi.org/10.1016/j.solidstatesciences.2019.03.012.

(19) Rabenau, A.; Rau, H. Über Sulfidhalogenide Des Bleis Und Das Pb4SeBr6. *ZAAC - J. Inorg. Gen. Chem.* **1969**, *369* (3–6), 295–305. https://doi.org/10.1002/zaac.19693690319.

(20) Ni, D.; Guo, S.; Powderly, K. M.; Zhong, R.; Cava, R. J. A High-Pressure Phase with a Non-Centrosymmetric Crystal Structure in the PbSe–PbBr2 System. *J. Solid State Chem.* **2019**, *280*. https://doi.org/10.1016/j.jssc.2019.120982.